Investigating Dilepton Production Rates and Polarization at Finite Baryon Density

Bailey Forster, Department of Physics
McGill University, Montreal
04, 2024

A thesis submitted to McGill University in partial fulfillment of the
requirements of the degree of

Master of Science

Abstract

Under extremely high energy conditions, constituents of nuclear matter become asymptotically free, forming a quark-gluon plasma (QGP). This state of matter is theorized to have existed in the very early universe and can be reproduced in relativistic heavy-ion collision experiments. The plasma rapidly cools, producing electromagnetic radiation throughout its evolution.

Photons and dileptons, unlike hadrons that interact strongly with the QGP, can carry information about the characteristics of the QGP medium at the time they were electromagnetically produced. Future experiments are aiming to measure dileptons in lower energy collisions where the net baryon density of the plasma is finite. As such, there is a need for theoretical predictions of dilepton yields in the context of finite net baryon density. Recently, next-to-leading-order (NLO) perturbative corrections with finite net baryon density have been calculated [1, 2]. Hydrodynamic models have been used to calculate the invariant mass spectrum of the total dilepton yield [3, 4]. Thus far, little work has been done on polarized dilepton emission and on the dilepton momentum distribution. The goal of this thesis is to take a step back and closely examine the 2D structure of the dilepton rates and their polarization with respect to both invariant mass and momentum.

Abrégé

Sous des conditions d'énergie extrêmement élevées, les constituants de la matière nucléaire deviennent asymptotiquement libres, formant un plasma de quarks et de gluons (QGP). On théorise que cet état de la matière a existé dans l'univers très jeune et peut être reproduit dans des expériences de collisions d'ions lourds relativistes. Le plasma se refroidit rapidement, produisant un rayonnement électromagnétique tout au long de son évolution.

Les photons et les dileptons, contrairement aux hadrons qui interagissent fortement avec le QGP, peuvent contenir des informations sur les caractéristiques du milieu du QGP au moment de leur production électromagnétique. Des expériences futures visent à mesurer les dileptons dans des collisions à plus basse énergie où la densité de baryons nette du plasma est finie. En tant que tel, il est nécessaire de prédire théoriquement la production de dileptons dans le contexte d'une densité de baryons nette finie. Récemment, des corrections perturbatives next-to-leading-order (NLO) avec une densité de baryons nette finie ont été calculées. Des modèles hydrodynamiques ont été utilisés pour calculer le spectre de masse invariante des dileptons. Jusqu'à présent, peu de travail a été fait sur l'émission de dileptons polarisés et sur la distribution de leur impulsion. Le but de cette

thèse est de prendre du recul et d’examiner de près la structure 2D des taux de dileptons et leur polarisation en fonction de la masse invariante et de l’impulsion.

Acknowledgements

First, I would like to thank my supervisor, Charles Gale, for his patience and guidance throughout this process. His insight and encouragement have helped me to grow as a physicist and to persist through setbacks in my research. I also benefited greatly from the opportunity to explore other topics of research and connect with students and experts in our field at an international summer school.

I am very grateful for the advice and support I've received from fellow members of the McGill Nuclear Theory Group, as well as our collaborators. Thank you especially to Jessica Churchill, for answering my many questions and helping to debug my code in the early days of this project. Greg Jackson generously shared his NLO rate calculations, which were essential to the work in this thesis, and Lipei Du provided the results of his hydrodynamic simulations at finite net baryon density.

Additionally, I would like to acknowledge that this degree was supported in part by a Canada Graduate Scholarship - Masters (2021-2022) from the Natural Sciences and Engineering Research Council of Canada (NSERC).

Finally, I am infinitely grateful for my family and friends for everything they have done to support me. I truly could not have finished this thesis without their care and encouragement.

Table of Contents

List of Figures

List of Abbreviations

ALICE A Large Ion Collider Experiment

CERN Organisation Européenne pour la Recherche Nucléaire (formerly "Conseil Européen pour la Recherche Nucléaire")

CM Center of Mass

FD Fermi-Dirac

HERA Hadron–Electron Ring Accelerator

HIC Heavy-Ion Collision

LHC Large Hadron Collider

LO Leading Order

LPM Landau–Pomeranchuk–Migdal

MB Maxwell-Boltzmann

MUSIC MUScl for Ion Collisions

NLO Next-to-Leading Order

NNLO Next-to-Next-to-Leading Order

pQCD Perturbative Quantum Chromodynamics

QCD Quantum Chromodynamics

QED Quantum Electrodynamics

QGP Quark-Gluon Plasma

RHIC Relativistic Heavy-Ion Collider

Chapter 1

Introduction

1.1 The Quark-Gluon Plasma

The aim of nuclear physics is to understand the fundamental constituents of matter and the forces that govern their interactions. For some time, it was thought that protons and neutrons were the most fundamental components of atomic nuclei. This changed with the introduction of the quark model, by Gell-Mann [5] and Zweig [6], and its experimental confirmation [7].

In the low temperature and density conditions of the present universe, quarks and gluons are tightly confined inside nucleons, which are themselves bound into atomic nuclei by the so called “strong” nuclear force. As such, an isolated quark has never been observed in nature. However, in the instant after the Big Bang, the extremely hot and dense conditions of the early universe allowed the formation of a new state of nuclear matter: the quark-gluon plasma (QGP) [8,9]. As the early universe cooled and expanded, this QGP gave rise to confined hadronic matter, eventually leading to the formation of the atoms, stars, and galaxies that exist in the present universe. While the evolution of the early universe cannot be observed directly, QGP has been produced in high energy experiments at particle colliders [10]. QGP formation may even occur naturally in the extremely dense cores of neutron stars, or in high energy astrophysical events such as neutron star mergers. Thus, the study of QGP and the strong interaction has important connections to cosmology and astrophysics, in addition to its fundamental interest in subatomic physics.

1.2 Quantum Chromodynamics

The strong nuclear force is one of four known fundamental forces, along with the electromagnetic, gravitational, and weak nuclear force. With the exception of gravity, each force has been described by a quantum field theory in which the interactions are mediated by virtual gauge bosons. In quantum electrodynamics (QED) it is the exchange of a photon that facilitates interactions between electrically charged particles. Experiments at CERN in 1983 confirmed the existence of the Z and W bosons that mediate the weak interactions [11].

As its name suggests, the strong nuclear force is most important in the context of understanding the interactions and phase transitions of nuclear matter, including the structure of hadrons and formation of the QGP. The strong force is described by the theory of quantum chromodynamics (QCD), in which quarks carry “colour” charge and interact through the exchange of gluons. While QED has only a single electrically neutral gauge boson, QCD has eight gluons which carry different combinations of colour charge. These colour-charged gluons are able to couple with themselves, a unique feature of QCD that allows for more complicated interactions than those of QED. QCD has three colour charges, commonly labelled "red", "blue", and "green". Analogous to light, combining the three colours creates a "white" or colour-neutral particle. Anti-quarks carry the corresponding anti-colours. Isolated colour charge is not seen in nature due to the strong interactions of QCD. Quarks are bound in colour neutral combinations to form hadrons, of which there are two types; baryons and mesons (and their antiparticles). Baryons consist of 3 quarks, one of each colour, while mesons have a quark and anti-quark with the corresponding colour and anti-colour charges.

Fritzsch, Gell-Mann, and Leutwyler developed the theory of QCD [12], and introduced the concept of colour charge as an SU(3) symmetry group [13] [1]. In the remainder of this section I will give a brief overview of the mathematical foundations of QCD, which are covered in detail in: [14, 15].

QCD is a non-abelian gauge theory with SU(3) symmetry. An early example of a non-abelian theory was introduced by Yang and Mills [16]. A defining property of such theories is that the generators are non-commutative. SU(3) has eight generators t^a which satisfy the commutation relationship

$$[t^a, t^b] = i f^{abc} t^c, \tag{1.1}$$

where f^{abc} are the structure constants, characteristic of the SU(3) algebra [14].

---

[1] This article discusses the history of QCD in more detail.

The QCD Lagrangian is given by [15]

$$\mathcal{L}_{QCD} = \bar{\psi}_i(i \not{\partial} - m)\delta_{ij}\psi_j - \frac{1}{4}F^a_{\mu\nu}F^{\mu\nu}_a + g\bar{\psi}_i\gamma^\mu A^a_\mu t^a_{ij}\psi_j, \tag{1.2}$$

where the gluon field strength is

$$F^a_{\mu\nu} = \partial_\mu A^a_\nu - \partial_\nu A^a_\mu + gf^{abc}A^b_\mu A^c_\nu. \tag{1.3}$$

This appears strikingly similar to the Lagrangian of QED [14]:

$$\mathcal{L}_{QED} = \bar{\psi}(i \not{\partial} - m)\psi - \frac{1}{4}F_{\mu\nu}F^{\mu\nu} + e\bar{\psi}\gamma^\mu A_\mu\psi. \tag{1.4}$$

In both cases, ψ represents the fermion field and A_μ are the gauge fields. Notice, however, in the QCD Lagrangian (Eq. (1.2)) the quark fields carry the indices $i, j = 1, 2, 3$, which indicate the colour of the field. The gauge fields and the field strength tensor also carry colour indices $(a, b, c...)$ which run from 1 to 8, representing the eight types of gluons. Repeated colour indices are summed over, as with Lorentz indices. Also, note that the QCD field strength, $F^a_{\mu\nu}$, differs from the QED field strength, $F_{\mu\nu}$, the consequences of which will be discussed later in this section.

The first term in Eq. (1.4) is the Dirac Lagrangian, which contains the kinetic energy term and mass m of the fermion field. This is followed by the kinetic term for the gauge fields, where the field strength tensor, $F_{\mu\nu}$, is a gauge invariant combination of A_μ. In QED, this is the electromagnetic field strength tensor $F_{\mu\nu} = \partial_\mu A_\nu - \partial_\nu A_\mu$ [14]. The final term is the interaction part of the QED Lagrangian. This describes the coupling of the

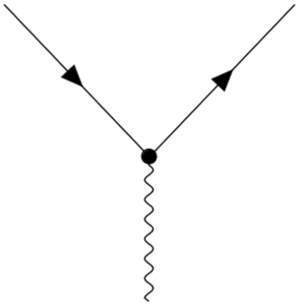

Figure 1.1: Feynman vertex of QED. Straight lines represent fermions and wavy lines represent photons.

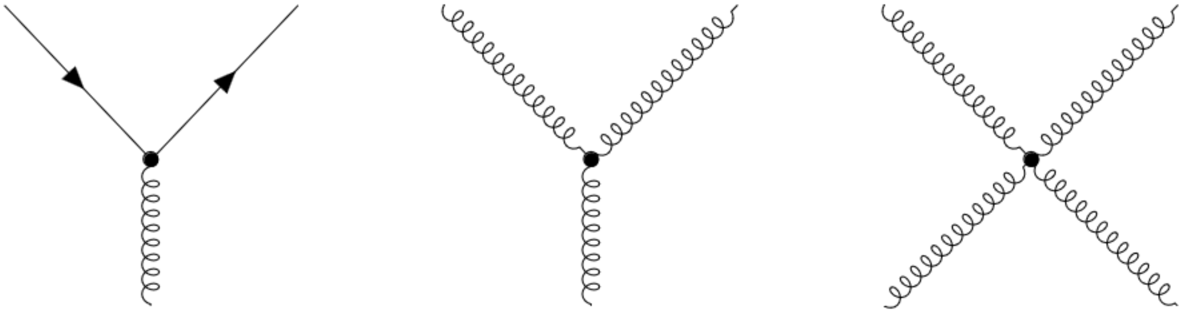

Figure 1.2: Feynman vertices of QCD. Straight lines represent fermions (quarks) and curly lines represent gluons. There are also contributions from non-physical ghost fields, which arise from the quantization of non-abelian theories, and depend on the choice of gauge. For example, see Appendix 1 in [14].

fermion and gauge fields, represented by the vertex diagram in Figure 1.1. This term carries the coupling constant, which, in the case of QED, is the fundamental electric charge e.

The QCD Lagrangian (Eq. (1.2)) has an analogous interaction term (Figure 1.2) which carries the coupling constant g. One can define $\alpha_s = g^2/4\pi$, similar to the fine structure constant of QED, $\alpha_{EM} = e^2/4\pi$. Note that natural units, $\hbar = c = \varepsilon_0 = 1$ are used. Here, the photon field is replaced with the gluon fields $A_\mu \to A_\mu^a t^a$. Summing over the colour index a produces a unique interaction term for each gluon species.

An important difference between the Lagrangians of QED and QCD is an additional interaction term that appears in the field strength tensor of QCD [17]. The gluon field strength (Eq. (1.3)) is derived from $[D_\mu, D_\nu] = -igF^a_{\mu,\nu}t^a$, where $D_\mu = \partial_\mu - igA^a_\mu t^a$ is the covariant derivative [14]. Thus, the additional term in $F^a_{\mu\nu}$ arises from the non-commutative properties (Eq. (1.1)) of the QCD generators t^a. This results in third and fourth order coupling of A^μ in the QCD Lagrangian, which is represented by the pure gluon interactions in Figure 1.2. These interactions have important implications for the behaviour of the strong force in different energy regimes.

1.3 QCD Phase Diagram

The strength of a force's interactions is determined by its coupling constant. The value of this "constant" actually depends on the energy scale of the interaction, which creates a "running coupling" [18]. QED is weakly interacting at low energy, and the coupling strength increases at higher energy. Interestingly, QCD coupling exhibits the opposite behaviour. Figure 1.3 shows the behaviour of the QCD coupling α_s with respect to the energy scale. At low energy, the coupling constant is large, and therefore the theory is strongly interacting. As energy increases, the coupling decreases logarithmically. This asymptotic freedom is a feature of non-abelian gauge theories, discovered by [19,20], and is a consequence of the gluon-gluon interactions [17], unique to QCD.

Characterization of the phases of nuclear matter in different energy regimes is an active area of research in nuclear physics. Figure 1.4 shows a schematic representation of the QCD phase diagram. At low to moderate temperature and baryon chemical poten-

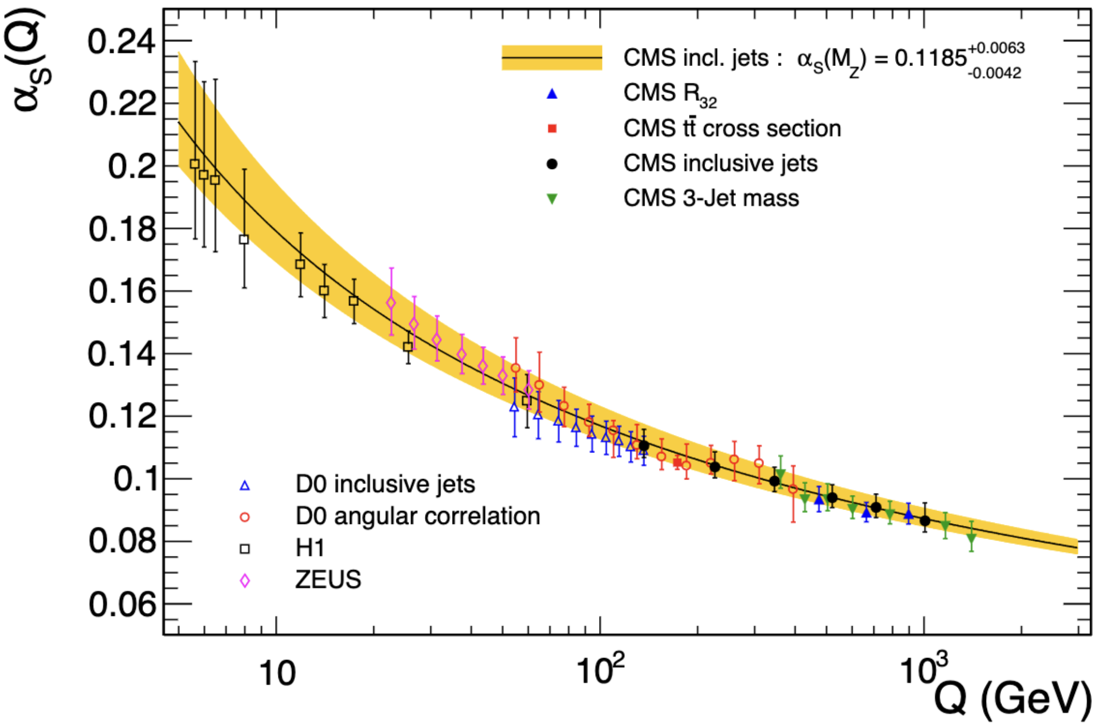

Figure 1.3: Measurement and pQCD predictions of the running coupling α_s as function of the energy scale Q, from [21].

tial, where α_s is large, the phase diagram indicates the confinement of quarks within hadronic matter. Binding of protons and neutrons into atomic nuclei occurs at very low temperature and moderate chemical potentials, where net baryon density is finite. As temperature increases, the coupling weakens. When the temperature is "high enough", asymptotic freedom allows the formation of QGP. The coupling of the QGP itself continues to decrease at even higher energies.

Different theoretical and experimental methods are needed to study the various regions of the phase diagram. In the weakly-coupled regime, perturbative methods can be used in theoretical calculations of QCD. However, at lower energies, α_s becomes too large for perturbative QCD (pQCD), so another method is needed. Lattice QCD is a numerical

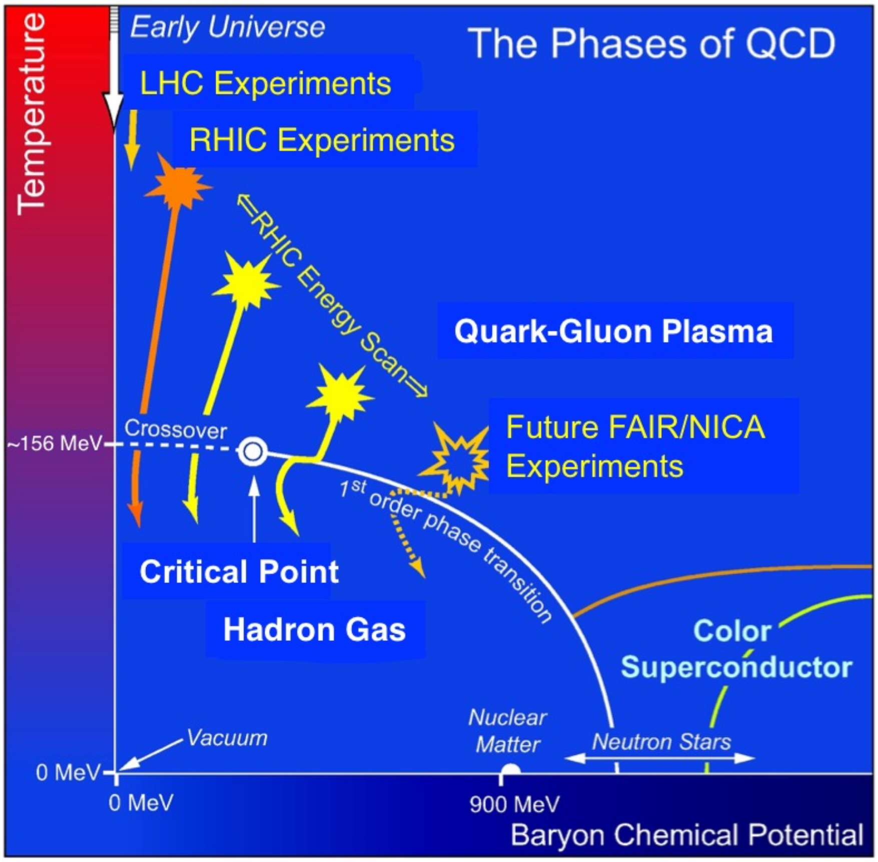

Figure 1.4: Phase Diagram of QCD taken from [22]. Temperature (T) is shown on the vertical axis and baryon chemical potential (μ_B) is shown on the horizontal axis. The crossover temperature, $T \sim 156$ MeV, is taken from [23].

method of evaluating path integrals, and has been successful at zero μ_B, but fails at finite net baryon density [24].

Because confinement leads to the impossibility of observing free quarks, it is difficult to directly detect QGP. In the present universe, QGP may occur in dense nuclear matter such as in the cores of neutron stars, or in binary mergers of compact stars. However, astrophysical observations are of limited use in studying the phase diagram of QCD since the energy conditions cannot be controlled. The best experimental method we have for mapping the high temperature QGP region of the phase diagram is to generate high energy collisions of large nuclei. Heavy-ion collision (HIC) experiments at the Relativistic Heavy-Ion Collider (RHIC) at Brookhaven National Laboratory and the Large Hadron Collider (LHC) at CERN are able to achieve extremely high energy conditions with very small net baryon density, similar to that of the early universe. Evidence of anisotropic flow in HIC experiments at RHIC, and later LHC, indicated the creation of a strongly interacting QGP state [10]. More recently, similar evidence of QGP formation has even been found in small systems, such as proton-proton collisions [25].

The QGP phase is extremely short lived, only lasting for ~ 10 fm/c [26], or approximately 10^{-23} seconds. Therefore, even in HIC experiments, it is challenging to measure QGP formation. We rely on indirect methods, by comparing measurements of particles produced in the collisions to theoretical models.

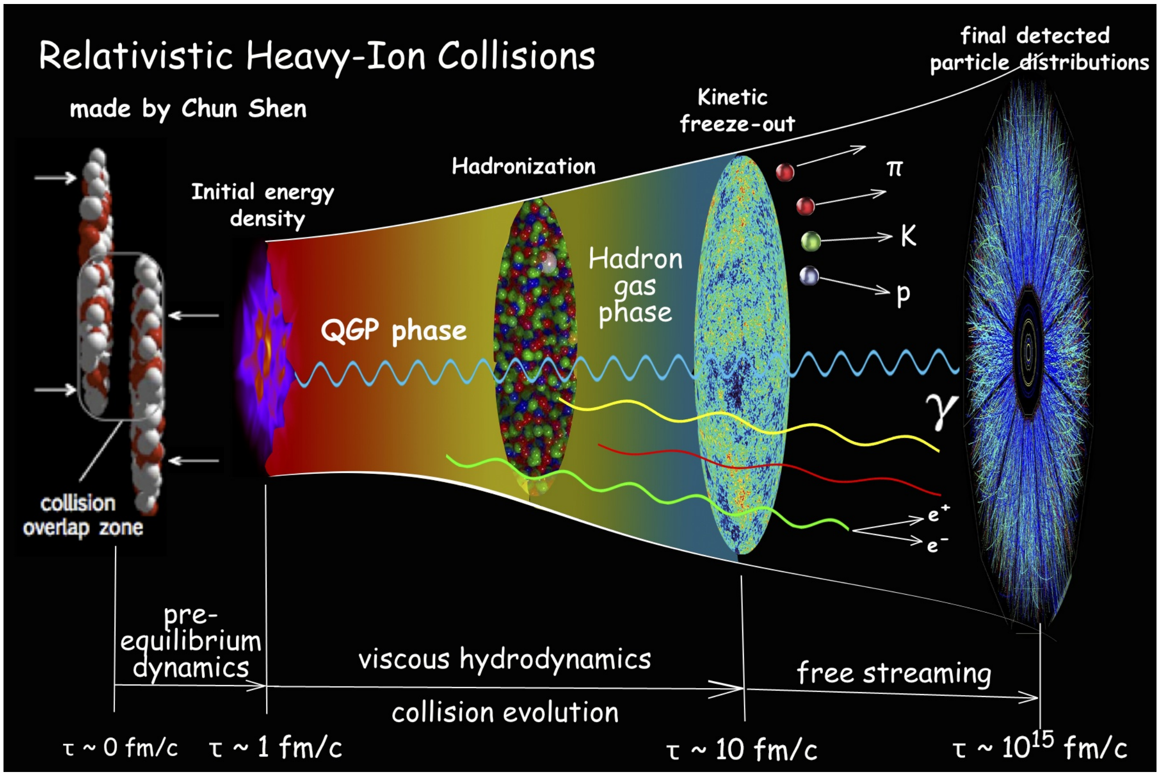

Figure 1.5: Stages of heavy-ion collisions taken from [27]. Time moves from left to right.

1.4 The Hybrid Model of Heavy-Ion Collisions

The evolution of HICs, depicted in Figure 1.5, can be described by a hybrid model consisting of five stages: the initial collision, pre-equilibrium, thermal QGP, hadronization, and freeze-out.

In the instant before the collision the nuclei are travelling at relativistic speeds. This results in Lorentz contraction in the Lab frame, as illustrated in Figure 1.5. Defining $R_N = R_0 A^{1/3} \sim 10$ fm as the nuclear radius[2], the thickness L of the Lorentz contracted nuclei is

$$L = 2R_N/\gamma. \tag{1.5}$$

The Lorentz factor can be calculated as

$$\gamma = \frac{E}{m} = \frac{\sqrt{s_{NN}}/2}{m}, \tag{1.6}$$

where E is the center of mass (CM) energy of a single nucleon and m is the nucleon mass, which is $m = 0.939$ GeV. The beam energy, $\sqrt{s_{NN}}$, is the total energy of a nucleon pair in the CM frame. Typical values of γ in HIC experiments are 106 for a beam energy of $\sqrt{s_{NN}} = 200$ GeV, and 1470 for $\sqrt{s_{NN}} = 2.76$ TeV. The thickness of the contracted nuclei would be ~ 0.2 fm and ~ 0.01 fm, respectively. Therefore, when the collision energy is sufficiently high, it can be assumed that the collision occurs simultaneously for all nucleons.

---

[2] $R_0 = 1.2$ fm, and A is the atomic number.

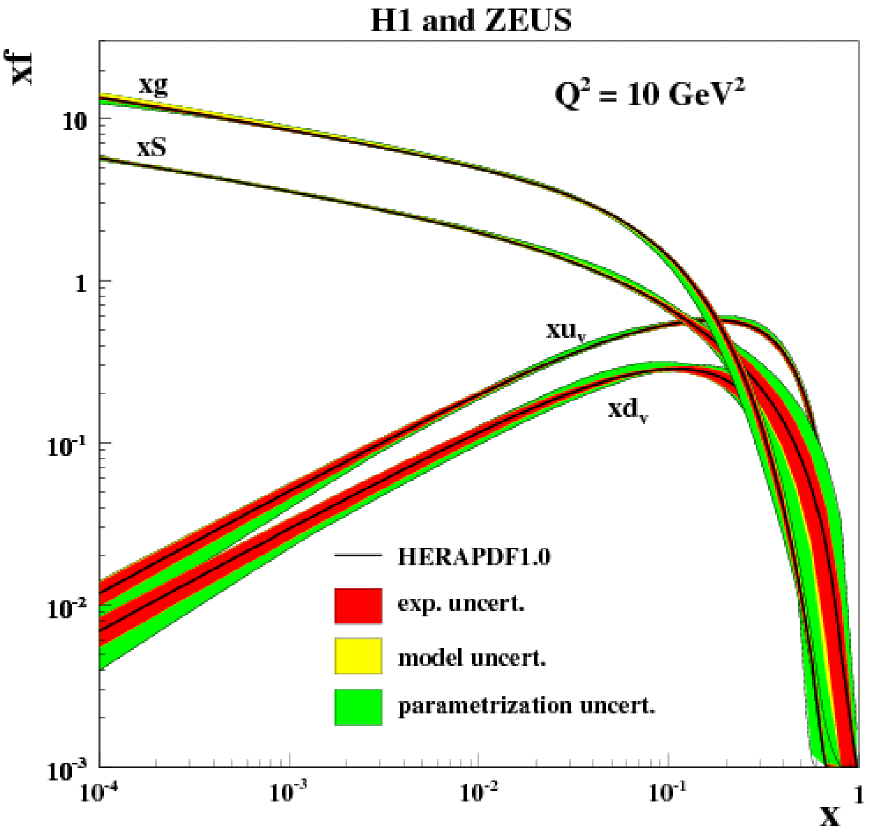

Figure 1.6: Quark and gluon distribution functions from Deep Inelastic Scattering experiments at HERA, taken from [28]. Distributions are shown with respect to the momentum fraction $x = p/\sqrt{s_{NN}}$. The gluon distribution function is labelled by xg, and quark distributions are xu_v (up), xd_v (down), and xS (sea quarks).

Higher energies also correspond to an increase in gluon density [29], as demonstrated by experimental measurements. Figure 1.6, for example, shows parton distribution functions fit to data from HERA [28]. The distributions are shown with respect to the parton momentum as a fraction of the beam energy, which is defined as $x = p/\sqrt{s_{NN}}$. These results show that gluon distribution becomes increasingly dominant towards small values of x, which is associated with higher beam energies. Therefore, the initial medium produced in high energy collisions can be modelled as a “pure-glue” plasma or “glasma”, and the initial gluon fields are evolved using the classical Yang-Mills equations [30].

The initial collision is followed by a pre-equilibrium stage, during which the medium evolves towards chemical and thermal equilibrium. The initially gluon dominated medium produces pairs of quarks and anti-quarks, resulting in a QGP with a nearly-zero net baryon density.

Close to thermal equilibrium, the QGP can be modelled as a near-ideal fluid [10], using simulations of viscous relativistic hydrodynamics, such as MUSIC [31]. Transport coefficients, such as shear and bulk viscosity, indicate how much the fluid deviates from equilibrium. In an ideal fluid these transport coefficients would be zero.

As the plasma expands and cools, the strength of the QCD coupling increases until the energy density is no longer sufficient to overcome the strong interactions. At this point, the medium enters the hadronization stage where the plasma condenses into a hadron gas. A method is needed to transition from the hydrodynamic description to distributions of hadron species. The Cooper-Frye prescription [32] is used to sample particle distributions based on the evolved stress-energy tensor at the time of freeze-out [10]. The newly formed hadrons interact and decay as the medium continues to expand. Kinetic freeze-out occurs when the mean free path becomes so large that the hadrons can free-stream to the detectors without any further interactions.

1.5 Electromagnetic Probes

Predictions of final particle yields are compared to experimental results in order to learn about the physics at each stage of the collision. It has been shown that hadronic observables are sensitive to transport coefficients of the hydrodynamic QGP medium, such as bulk and shear viscosity [33,34]. Therefore, these parameters can be extracted by fitting to hadron data. However, because of their participation in strong QCD interactions, hadron yields are mostly influenced by the late collision stages. A different method is needed to highlight the properties of the early QGP medium.

Electromagnetic radiation, in the form of direct photons and dileptons, is produced throughout all stages of the collision. Most importantly, photons and leptons do not carry colour charge, and therefore do not participate in strongly coupled QCD interactions as they propagate through the QGP medium. Since QED interactions are comparatively weak, the original signal will reach the detector mostly undisturbed. Therefore, electromagnetic probes are excellent candidates for learning about the characteristics at each stage of QGP formation and evolution.

Dileptons, in particular, have a wide range of applications [35, 36], because of the Lorentz invariance of their mass spectrum. These include measurements of the QGP lifetime [37] and extraction of average temperature from the invariant mass spectrum [38]. While current HIC experiments produce QGP with near-zero μ_B, future low energy experiments will probe the finite μ_B region of the QCD phase diagram [35]. Theoretical models of dilepton production at low energy are needed for comparison to these experiments.

The impact of including a pre-equilibrium model, K$\not{o}$MP$\not{o}$ST, between the initial glasma stage and the hydrodynamic QGP stage, has recently been studied [39]. It was found that the effect of K$\not{o}$MP$\not{o}$ST on photon observables is small. However, from a theoretical perspective it is important to provide a transition from the long mean free path in the initial gluon dominated medium to the short mean free path in the strongly interacting QGP fluid. In the future, a similar study could be performed to test the effect of K$\not{o}$MP$\not{o}$ST on the total dilepton yield across the pre-equilibrium, hydrodynamic, and hadronic stages. However, as a precursor, this thesis will focus on dilepton production rates in the thermal stage only.

Invariant mass spectra of photons and dileptons have recently been calculated from next-to-leading order (NLO) perturbative QCD rates[3] using (2+1)D hydrodynamic simulations [3]. The same work also briefly discussed the inclusion of finite μ_B. Notably, polarization has not yet been studied in the context of finite μ_B, and will be investigated in this work. Additionally, most simulations of dilepton production have focused on the p_T integrated invariant mass spectrum of the yield.

The goal of this thesis will be to provide an in-depth analysis of the differential M and p_T dependence of the dilepton rates. The effect of finite μ_B will be investigated for the total and polarized rates at LO and NLO. Chapter 2 introduces the derivation of thermal dilepton rates in kinetic theory. The leading order dilepton rate is re-derived in the Maxwell-Boltzmann limit and compared to the result obtained using proper Fermi-Dirac statistics. In Section 2.3.3, this is generalized to finite net baryon density ($\mu_B \neq 0$). Chapter 3 gives a brief overview of the field theory approach to calculating the dilepton rates

---

[3] Next-to-leading order perturbative QCD rates are discussed in 3.1.3.

from the photon self-energy and reviews the recent developments in NLO pQCD calculations of the photon spectral functions [1, 2, 40, 41]. The 2D differential rates are then compared at LO and NLO, and the effect of finite μ_B is analyzed. In Chapter 4, the same investigation is performed for the polarized components of the dilepton rates.

Chapter 2

Thermal Dilepton Production

2.1 Cross Section of Quark Pair Annihilation

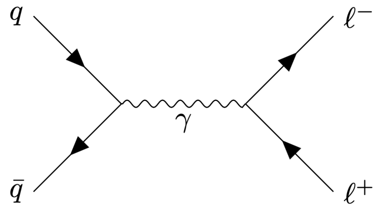

Figure 2.1: LO Feynman diagram for dilepton production from $q\bar{q}$ annihilation.

Dileptons are produced at all stages of the collision, predominantly through the annihilation of quark and anti-quark pairs, producing a virtual photon, which results in a pair of leptons. At leading order (LO) this is a purely QED process, and is represented by the Feynman diagram in Figure 2.1.

Calculating the cross section for Figure 2.1 gives

$$\sigma_{q\bar{q}} = F_q \frac{4\pi}{3} \frac{\alpha_{em}^2}{M^2} \left(1 + \frac{2m_l^2}{M^2}\right) \left(1 - \frac{4m_l^2}{M^2}\right)^{1/2}, \tag{2.1}$$

which agrees with the result in [42]. M is the CM energy of the dileptons (see definition in Eq. (2.11)), which is also referred to as the invariant mass. F_q includes the colour factor of $N_c = 3$, a spin factor, and a sum over the squared charge fraction e_f^2 of each quark flavour to modify the α_{em}^2 coefficient, which comes from assuming a fermion charge of $\pm e$ in the QED coupling constant:

$$F_q = N_c(2s+1)^2 \sum_f e_f^2. \tag{2.2}$$

The following derivations will assume the presence of 3 quark flavours: up, down, and strange, so that $F_q = 24/3 = 8$. Additionally, I will focus on di-electrons in this thesis, and thus it can be assumed that $m_l << M$, so Eq. (2.1) reduces to

$$\sigma_{q\bar{q}} = F_q \frac{4\pi}{3} \frac{\alpha_{em}^2}{M^2} = \frac{32\pi}{3} \frac{\alpha_{em}^2}{M^2}. \tag{2.3}$$

2.2 Total Rate from Kinetic Theory

I will start by defining the total dilepton production rate R, which is the number of dilepton pairs produced per unit of spacetime in (3+1)D.

$$R \equiv \frac{dN}{d^4X} = \frac{dN}{dt d^3\mathbf{x}} \tag{2.4}$$

In kinetic theory, the rate calculation involves integrating the probability $|\mathcal{M}|^2$ of a single interaction over the momentum distributions $f(\mathbf{p}_i)$ of the initial particles and the phase space of the final state that is permitted by energy-momentum conservation. At leading order (LO) in α_{EM}, quark-antiquark annihilation ($q\bar{q} \to \ell^+\ell^-$), shown in Figure 2.1, is the only proccess contributing to dilepton production. Neglecting possible final state effects such as Pauli blocking and Bose-Einstein enhancement, the general rate for a two-body scattering process ($1+2 \rightarrow 3+4$) is [43]

$$R = \int \frac{d^3\mathbf{p}_1}{2E_1(2\pi)^3}\frac{d^3\mathbf{p}_2}{2E_2(2\pi)^3}\frac{d^3\mathbf{p}_3}{2E_3(2\pi)^3}\frac{d^3\mathbf{p}_4}{2E_4(2\pi)^3} f(\mathbf{p}_1)f(\mathbf{p}_2)|\mathcal{M}|^2(2\pi)^4\delta^4(P_1+P_2-P_3-P_4). \tag{2.5}$$

At thermal equilibrium, the parton distribution functions should be isotropic and depend only on the magnitude of momentum, so $f(\mathbf{p}_i) \rightarrow f(|\mathbf{p}_i|)$. See the next page for definitions of the energy and momentum variables in Eq. (2.5).

Attempting to integrate Eq. (2.5) directly in the lab frame results in some complicated angular dependencies. However, the calculation can be simplified by evaluating the invariant part of this expression in the centre of mass frame.

Recalling the Lorentz invariant cross section for two-body scattering [44]

$$\sigma_{1+2\rightarrow 3+4} = \frac{1}{\sqrt{(P_1\cdot P_2)^2 - m_q^4}}\int \frac{d^3\mathbf{p}_3}{2E_3(2\pi)^3}\frac{d^3\mathbf{p}_4}{2E_4(2\pi)^3}|\mathcal{M}|^2(2\pi)^4\delta^4(P_1+P_2-P_3-P_4), \tag{2.6}$$

where m_1 and m_2 have been replaced with the quark mass m_q, and defining the relativistic relative velocity of the initial quarks

$$v_{rel} = \frac{\sqrt{(P_1\cdot P_2)^2 - m_q^4}}{E_1E_2}, \tag{2.7}$$

the production rate in Eq. (2.5) can be rewritten as

$$R = \int \frac{d^3\mathbf{p}_1}{(2\pi)^3}\frac{d^3\mathbf{p}_2}{(2\pi)^3} f(\mathbf{p}_1) f(\mathbf{p}_2) \sigma_{q\bar{q}} v_{rel}. \tag{2.8}$$

This is the definition used in [42], and will be the starting point of the derivation in the following section.

2.3 Differential Rate

Consider a quark-antiquark pair with energies E_1, E_2, and three-momentum $\mathbf{p}_1$, $\mathbf{p}_2$, so that the total energy and three-momentum are defined as:

$$\begin{aligned} E &= E_1 + E_2 \\ \mathbf{p} &= \mathbf{p}_1 + \mathbf{p}_2. \end{aligned} \tag{2.9}$$

In this work, four-vectors will be represented by capital letters, and the metric signature will be mostly minus (+ - - -). The four-momenta of the two quarks are $P_1 = (E, \mathbf{p}_1)$ and $P_2 = (E, \mathbf{p}_2)$. The total four-momentum, $P = P_1 + P_2$, has the components:

$$P^\mu = (p^0, p^1, p^2, p^3) = (E, \mathbf{p}). \tag{2.10}$$

From here, one can define the Lorentz invariant mass

$$M^2 \equiv P^\mu P_\mu = P^2 = (P_1 + P_2)^2. \tag{2.11}$$

Experiments can determine the invariant mass and the momentum of the dileptons captured by the detectors, therefore, we can extract more information about the system by looking at the differential rate.

The total rate in Eq. (2.8) can be rewritten in the differential form $dR/dM^2d^3\mathbf{p}$, using the definition of invariant mass (Eq. (2.11)) and the total 3-momentum of the initial quarks (Eq. (2.9)):

$$\frac{dR}{dM^2d^3\mathbf{p}} = \int \frac{d^3\mathbf{p}_1}{(2\pi)^3}\frac{d^3\mathbf{p}_2}{(2\pi)^3} f(p_1)f(p_2)\sigma_{q\bar{q}}v_{rel}\delta(M^2 - (P_1 + P_2)^2)\delta^3(\mathbf{p} - (\mathbf{p}_1 + \mathbf{p}_2)). \tag{2.12}$$

The differential rate is often written in another form with respect to the total 4-momentum

$$\frac{dR}{d^4P} = \frac{dR}{dEd^3\mathbf{p}}, \tag{2.13}$$

which is related to the rate in Eq. (2.12) using $dM^2 = 2EdE$, so that

$$\frac{dR}{d^4P} = 2E\frac{dR}{dM^2d^3\mathbf{p}}. \tag{2.14}$$

As discussed in the previous section, three quark species (up, down, strange) will be used in this calculation. The masses of these quarks are sufficiently small that the quarks may be assumed to be massless, so that $E_1 \approx |\mathbf{p_1}| \equiv p_1$ and $E_2 \approx |\mathbf{p_2}| \equiv p_2$. In this limit, the relative velocity of the quarks defined in Eq. (2.7) becomes $v_{rel} \approx \frac{|P_1 \cdot P_2|}{E_1E_2}$, and the argument of the first delta function can also be simplified using $(P_1 + P_2)^2 \approx 2(P_1 \cdot P_2)$.

Now the differential dilepton production rate for massless quarks is

$$\frac{dR}{dM^2 d^3\mathbf{p}} = \int \frac{d^3\mathbf{p}_1}{(2\pi)^3}\frac{d^3\mathbf{p}_2}{(2\pi)^3} f(E_1)f(E_2)\sigma_{q\bar{q}}\frac{|P_1\cdot P_2|}{E_1E_2}\delta(M^2-2(P_1\cdot P_2))\delta^3(\mathbf{p}-(\mathbf{p}_1+\mathbf{p}_2)). \quad (2.15)$$

First, integrating over $\mathbf{p}_2$, using $\delta^3(\mathbf{p}-\mathbf{p}_1-\mathbf{p}_2)$ gives

$$\frac{dR}{dM^2 d^3\mathbf{p}} = \frac{1}{(2\pi)^6}\int d^3\mathbf{p_1} f(E_1)f(\bar{E}_2)\sigma_{q\bar{q}}\frac{|P_1\cdot \bar{P}_2|}{E_1\bar{E}_2}\delta(M^2-2(P_1\cdot P_2)). \quad (2.16)$$

From the delta function, $\mathbf{p_2}=\mathbf{p}-\mathbf{p_1}$, so I replace $E_2\to\bar{E}_2$ and $P_2\to\bar{P}_2$, where

$$\begin{aligned}\bar{E}_2 &= |\mathbf{p}_2| = |\mathbf{p}-\mathbf{p}_1| = \sqrt{p^2+p_1^2-2\mathbf{p}_1\cdot\mathbf{p}}\\ P_1\cdot\bar{P}_2 &= E_1\bar{E}_2-\mathbf{p}_1\cdot\mathbf{p}+p_1^2.\end{aligned} \quad (2.17)$$

For the integration over $\mathbf{p_1}$, I choose a spherical coordinate system with $\mathbf{p}$ on the z axis

$$\begin{aligned}\mathbf{p} &= p(0,0,1)\\ \mathbf{p}_1 &= p_1(\sin\theta_1\cos\phi_1, \sin\theta_1\sin\phi_1, \cos\theta_1)\\ d^3\mathbf{p}_1 &= p_1^2\sin\theta_1 dp_1 d\theta_1 d\phi_1.\end{aligned} \quad (2.18)$$

With this choice of coordinates, the integrand has no dependence on ϕ_1 since $\mathbf{p}_1$ only appears in the dot product $\mathbf{p_1}\cdot\mathbf{p}=|\mathbf{p_1}||\mathbf{p}|\cos\theta_1$. Therefore, integrating over the azimuthal angle gives a factor of 2π.

Now Eq. (2.16) becomes

$$\frac{dR}{dM^2 d^3\mathbf{p}} = \frac{1}{(2\pi)^5}\int_0^\infty \int_0^\pi p_1^2 \sin\theta_1 dp_1 d\theta_1 f(E_1) f(\bar{E}_2)\sigma_{q\bar{q}}\frac{|P_1\cdot\bar{P}_2|}{E_1\bar{E}_2}\delta(M^2 - 2(P_1\cdot\bar{P}_2)). \quad (2.19)$$

Recall that for massless quarks $p_1 \approx E_1$, and thus the integration measure can be rewritten with $dp_1 \to dE_1$. Then, defining a change of variables, $\chi = \cos\theta_1$ and $d\chi = -\sin\theta_1 d\theta_1$, and reversing the integration limits gives

$$\frac{dR}{dM^2 d^3\mathbf{p}} = \frac{1}{(2\pi)^5}\int_0^\infty \int_{-1}^1 dE_1 d\chi f(E_1) f(\bar{E}_2)\sigma_{q\bar{q}}|P_1\cdot\bar{P}_2|\frac{E_1}{\bar{E}_2}\delta(M^2 - 2(P_1\cdot\bar{P}_2)). \quad (2.20)$$

Evaluating Eq. (2.17) with this change of variables, we have

$$\begin{aligned} \bar{E}_2 &= \sqrt{E_1^2 + p^2 - 2E_1 p\chi} \\ P_1\cdot\bar{P}_2 &= E_1\bar{E}_2 - E_1 p\chi + E_1^2. \end{aligned} \quad (2.21)$$

The integration over χ is performed using the remaining delta function, which must first be rewritten in the form

$$\delta(g(\chi)) = \sum_i \frac{\delta(\chi - \chi_i)}{|g'(\chi_i)]}, \quad (2.22)$$

where χ_i are the zeros of $g(\chi) = M^2 - 2(P_1\cdot\bar{P}_2)$.

Substituting Eq. (2.21) and solving $g(\chi) = 0$ yields two solutions:

$$\chi_\pm = \frac{-M^2 \pm 2E_1 E}{2E_1 p}. \quad (2.23)$$

Given that $E = \sqrt{M^2 + p^2} \geq p$, it is always the case that $\chi_- \leq -1$. Therefore, only the χ_+ solution is supported on the integration region $\chi : [-1, 1]$, and the delta function can be replaced with

$$\delta(g(\chi)) = \frac{\delta(\chi - \chi_+)}{|g'(\chi_+)|}. \tag{2.24}$$

Performing the χ integration gives the following:

$$\frac{dR}{dM^2 d^3\mathbf{p}} = \frac{\sigma_{q\bar{q}}}{(2\pi)^5} \int_0^\infty dE_1 \left[f(E_1) f(\bar{E}_2) |P_1 \cdot \bar{P}_2| \frac{E_1}{\bar{E}_2} \frac{1}{|g'(\chi)|} \right]_{\chi=\chi_+} \Theta(1 - |\chi_+|), \tag{2.25}$$

where the step function $\Theta(1 - |\chi_+|)$ comes from the fact that the delta function is only supported on part of the region of integration; specifically, where $|\chi_+| < 1$.

The Jacobian

$$\begin{aligned} |g'(\chi)| &= \left| \frac{\partial}{\partial\chi} (M^2 - 2(E_1\bar{E}_2 - E_1 p \chi + E_1^2)) \right| \\ &= \left| 2E_1 (-\frac{\partial \bar{E}_2}{\partial \chi} + p) \right| \\ &= \left| 2p \frac{E_1}{\bar{E}_2} (E_1 + \bar{E}_2) \right| \end{aligned} \tag{2.26}$$

is substituted into Eq. (2.25).

$$\frac{dR}{dM^2 d^3\mathbf{p}} = \frac{\sigma_{q\bar{q}}}{(2\pi)^5} \int_0^\infty dE_1 \left[f(E_1) f(\bar{E}_2) \frac{|P_1 \cdot \bar{P}_2|}{2p(E_1 + \bar{E}_2)} \right]_{\chi=\chi_+} \Theta(1 - |\chi_+|) \tag{2.27}$$

The boundaries of the E_1 integration region are determined by solving the argument of the step function, to get:

$$E_{1max} = \frac{E+p}{2} \tag{2.28}$$
$$E_{1min} = \frac{E-p}{2}. \tag{2.29}$$

After replacing $\chi \to \chi_+$ in the integrand, so that $\bar{E}_2|_{\chi+} = E - E_1$ and $(P_1 \cdot \bar{P}_2)|_{\chi+} = \frac{M^2}{2}$, the only remaining step is to integrate the thermal distribution functions over E_1:

$$\frac{dR}{dM^2 d^3\mathbf{p}} = \frac{\sigma_{q\bar{q}}}{(2\pi)^5} \frac{M^2}{4pE} \int_{E_{1min}}^{E_{1max}} dE_1 f(E_1) f(E - E_1). \tag{2.30}$$

2.3.1 Maxwell-Boltzmann Rate

When the energy of a particle is much larger than the temperature, or $E_i/T >> 1$, the Maxwell-Boltzmann (MB) distribution function, $f_{MB}(E_i) = e^{-E_i/T}$, can be used. So, in this limit, the integrand of Eq. (2.30) becomes $f(E_1)f(E-E_1) = e^{-E_1/T}e^{-(E-E_1)/T} = e^{-E/T}$, and after performing the straightforward integration over E_1, the approximated differential rate is

$$\frac{dR}{dM^2 d^3\mathbf{p}} = \frac{\sigma_{q\bar{q}}}{(2\pi)^5} \frac{M^2}{4E} e^{-E/T}. \tag{2.31}$$

2.3.2 Fermi-Dirac Rate

As fermions, the quark and anti-quark distributions in the thermal QGP are more accurately characterized by Fermi-Dirac (FD) statistics. In this case

$$f(E_1)f(E-E_1) = \left(\frac{1}{e^{E_1/T}+1}\right)\left(\frac{1}{e^{(E-E_1)/T}+1}\right). \tag{2.32}$$

Again, an analytical result can be obtained for the E_1 integration:

$$\int_{E_{1min}}^{E_{1max}} dE_1 \left(\frac{1}{e^{E_1/T}+1}\right)\left(\frac{1}{e^{(E-E_1)/T}+1}\right) = \frac{T}{(e^{E/T}-1)} \ln\left[\frac{1+e^{E_1/T}}{e^{E/T}+e^{E_1/T}}\right]_{E_{1min}}^{E_{1max}}. \tag{2.33}$$

Evaluating with the integration limits defined in Eq. (2.29), the logarithmic term becomes

$$\ln\left[\frac{\left(1+e^{\frac{1}{T}(E/2+p/2)}\right)}{\left(e^{E/T}+e^{\frac{1}{T}(E/2+p/2)}\right)}\frac{\left(e^{E/T}+e^{\frac{1}{T}(E/2-p/2)}\right)}{\left(1+e^{\frac{1}{T}(E/2-p/2)}\right)}\right]. \tag{2.34}$$

This can be simplified by expanding and cancelling a factor of $e^{E/T}$ to get

$$\ln\left[\frac{e^{-(E+p)/2T}+e^{(E+p)/2T}+2}{e^{(E-p)/2T}+e^{-(E-p)/2T}+2}\right]. \tag{2.35}$$

Now the exponential terms can easily be replaced with the hyperbolic function, $\cosh(x) = (e^x+e^{-x})/2$:

$$\ln\left[\frac{\cosh\left((E+p)/2T\right)+1}{\cosh\left((E-p)/2T\right)+1}\right]. \tag{2.36}$$

And finally, using the double angle identity, the differential rate simplifies to

$$\frac{dR}{dM^2 d^3\mathbf{p}} = \frac{\sigma_{q\bar{q}}}{(2\pi)^5} \frac{M^2}{4pE} \frac{2T}{\left(e^{E/T}-1\right)} \ln\left[\frac{\cosh\left((E+p)/4T\right)}{\cosh\left((E-p)/4T\right)}\right]. \tag{2.37}$$

2.3.3 Finite Chemical Potential

Collisions at very high RHIC and LHC energies probe the high temperature but low baryon potential, μ_B, region of the QCD phase diagram. In Section 1.4, I discussed how the production of quark-antiquark pairs from the dominant gluon distributions in high energy experiments results in near-zero net baryon density. However, at lower energies, the gluon distributions reduce dramatically and fewer quark-antiquark pairs are produced. Therefore, the contribution of the quarks that were present in the original nuclei is no longer negligible. This results in a system with asymmetric quark and anti-quark distributions.

Each of the quark distribution functions in Eq. (2.30) is modified by a chemical potential μ_i.

$$f_{MB}(E_i) = e^{-(E_i-\mu_i)/T} \tag{2.38}$$

$$f_{FD}(E_i) = \frac{1}{e^{(E_i-\mu_i)/T}+1} \tag{2.39}$$

The quark chemical potential, $\mu = \frac{\partial U}{\partial N}$, is defined as the rate of change of the internal energy, U, of the system with respect to the change in the net quark number, $N = N_q - N_{\bar{q}}$. This is related to the net baryon chemical potential, $\mu_B = 3\mu$. A chemical potential of $\mu = 0$ indicates an equal distribution of quarks and anti-quarks, and $\mu > 0$ means that there are more quarks than anti-quarks. If we choose $f(E_1)$ as the quark distribution, then $\mu_1 = \mu$, and the anti-quark potential has the opposite sign, $\mu_2 = -\mu$. Interestingly, μ has no effect on the rate in the MB approximation. The $\pm\mu$ terms cancel and the integrand of Eq. (2.30) is the same as in Section 2.3.1:

$$f(E_1)f(E-E_1) = e^{-(E_1-\mu)/T}e^{-(E-E_1+\mu)/T} = e^{-E/T}. \tag{2.40}$$

Now, returning to the Fermi-Dirac rates, the integrand is

$$f(E_1)f(E-E_1) = \left(\frac{1}{e^{(E_1-\mu)/T}+1}\right)\left(\frac{1}{e^{(E-E_1+\mu)/T}+1}\right). \tag{2.41}$$

Integrating Eq. (2.30) over E_1 and simplifying, similarly to the previous section, produces

$$\frac{dR}{dM^2d^3\mathbf{p}} = \frac{\sigma_{q\bar{q}}}{(2\pi)^5}\frac{M^2}{4pE}\frac{T}{(e^{E/T}-1)}\ln\left[\frac{\cosh\left((E+p)/2T\right)+\cosh\left(\mu/T\right)}{\cosh\left((E-p)/2T\right)+\cosh\left(\mu/T\right)}\right]. \tag{2.42}$$

These results are compared to the MB approximation in Figure 2.2 in the next section.

A similar result for dR/d^4P has been derived in [45]. To compare my derivation to that of [45], I use Eq. (2.14) and the cross section in Eq. (2.3), but with $F_q = 20/3$ for up and down quarks only.

$$\frac{dR}{d^4P} = \frac{5\alpha_{em}^2}{36\pi^4}\frac{1}{p}\frac{T}{(e^{E/T}-1)}\ln\left[\frac{\cosh\left((E+p)/2T\right)+\cosh\left(\mu/T\right)}{\cosh\left((E-p)/2T\right)+\cosh\left(\mu/T\right)}\right] \tag{2.43}$$

My result in Eq. (2.43) is an equivalent but simplified form of equation (7) from [45], which is

$$\frac{dR}{d^4P} = \frac{5\alpha_{em}^2}{36\pi^4}\frac{T}{p}\left(\frac{1}{e^{E/T}-1}\right)\ln\left[\frac{\cosh^2((p+E)/4T) - \tanh^2(\mu/2T)\sinh^2((p+E)/4T)}{\cosh^2((p-E)/4T) - \tanh^2(\mu/2T)\sinh^2((p-E)/4T)}\right]. \tag{2.44}$$

The argument of this log function can be simplified with a few trig identities. First, using $\tanh^2(\mu/2T) = 1 - \text{sech}^2(\mu/2T)$, expanding, and replacing $\cosh^2((p-E)/4T) - \sinh^2((p-E)/4T) = 1$, I get

$$\frac{1 + \text{sech}^2(\mu/2T)\sinh^2((p+E)/4T)}{1 + \text{sech}^2(\mu/2T)\sinh^2((p-E)/4T)}. \tag{2.45}$$

Now, multiplying the numerator and denominator by $\cosh^2(\mu/2T)$

$$\frac{\cosh^2(\mu/2T) + \sinh^2((p+E)/4T)}{\cosh^2(\mu/2T) + \sinh^2((p-E)/4T)} \tag{2.46}$$

Finally, applying the hyperbolic half angle identities, I obtain an equivalent expression to the logarithmic argument in Eq (2.43)

$$\frac{\cosh(\mu/T) + \cosh((p+E)/2T)}{\cosh(\mu/T) + \cosh((p-E)/2T)}. \tag{2.47}$$

2.3.4 Dilepton Rates at Mid-Rapidity

In the previous sections I derived the dilepton rate $dR/dM^2d^3\mathbf{p}$ which is related to the differential rate with respect to the total 4-momentum of the dileptons,

$$\frac{dR}{d^4P} = \frac{dR}{dEd^3\mathbf{p}} = 2E\frac{dR}{dM^2d^3\mathbf{p}}. \tag{2.48}$$

In heavy-ion collisions, nuclei collide at relativistic speeds and produce particles that propagate in all directions. It is natural to describe this system in cylindrical coordinates, with the z-axis being the direction of the collision.

$$d^3\mathbf{p} = p_T dp_T d\phi dp_z \tag{2.49}$$

At very high collision energies, the momentum in the z direction is much greater than in the transverse direction. Typically, p_z is replaced with a logarithmic quantity, the rapidity, which is defined as:

$$y = \frac{1}{2} ln\left(\frac{E+p_z}{E-p_z}\right). \tag{2.50}$$

With this change of variables, the integration measure becomes

$$d^3\mathbf{p} = Ep_T dp_T d\phi dy. \tag{2.51}$$

Using Eq. (2.51) and $dM^2 = 2MdM$, Eq. (2.48) can be rewritten as

$$\frac{dR}{d^4P} = \frac{1}{Mp_T}\frac{dR}{dMdp_Td\phi dy}.$$

Then rearranging, we have

$$\frac{dR}{dMdp_Tdy} = \int d\phi M p_T \frac{dR}{d^4P}. \tag{2.52}$$

Here, ϕ is the angle of p_T in transverse plane. Therefore, using the azimuthal symmetry of the system, integrating over ϕ gives a factor of 2π. So now we have

$$\frac{dR}{dMdp_Tdy} = 2\pi M p_T \frac{dR}{d^4P}. \tag{2.53}$$

This work will focus on the dilepton production at mid-rapidity ($y = 0$), which corresponds to $p_z = 0$, so that $p = p_T$. At mid-rapidity, the differential rate with respect M and p_T is given by

$$\left.\frac{dR}{dMdp_Tdy}\right|_{y=0} = 2\pi M p_T \left.\left(\frac{dR}{d^4P}\right)\right|_{p=p_T}. \tag{2.54}$$

Often, the rate is also integrated over p_T to obtain the Lorentz invariant mass spectrum:

$$\left.\frac{dR}{dMdy}\right|_{y=0} = 2\pi \int dp_T M p_T \left.\left(\frac{dR}{d^4P}\right)\right|_{p=p_T}. \tag{2.55}$$

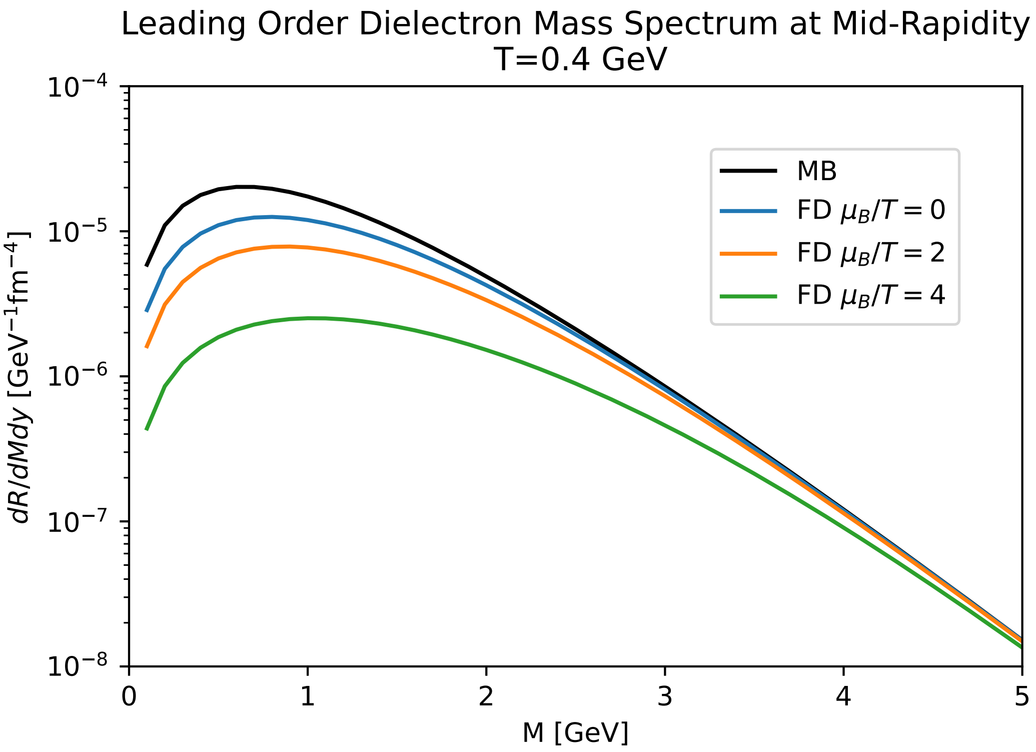

Figure 2.2: The p_T integrated dielectron mass spectrum at mid-rapidity and $T = 0.4$ GeV. The Maxwell-Boltzmann (MB) approximation (black) is compared to results from Fermi-Dirac (FD) statistics with finite $\mu_B/T = 0, 2, 4$.

For the Maxwell-Boltzmann case this integration can be performed analytically to get

$$\left.\frac{dR}{dMdy}\right|_{y=0} = \frac{\sigma_{q\bar{q}}M^2}{4(2\pi)^4}T^2\left(1 + M/T\right)e^{-M/T} = \frac{\alpha_{EM}^2}{6(2\pi)^3}T^2\left(1 + M/T\right)e^{-M/T}, \tag{2.56}$$

where $\sigma_{q\bar{q}}$ is replaced with the small m_q approximation in Eq. (2.3). However, in the Fermi-Dirac case, the integration over p_T must be performed numerically.

Figure 2.2 shows the Fermi-Dirac results for the mid-rapidity mass spectrum evaluated at $T = 0.4$ GeV and $\mu_B/T = 0, 2, 4$. These results are compared to the Maxwell-Boltzmann approximation in Eq. (2.56). As expected, the MB and FD rates converge at high M, since $M^2 = (P_1+P_2)^2 \approx 2E_1E_2(1-\hat{p_1}\cdot\hat{p_2})$ is large when the quark energies, E_1 and

E_2, are large. At $\mu_B = 0$, the MB approximation only requires that $E_i >> T$. In Figure 2.2, the FD and MB spectra at $\mu_B = 0$ converge at $\sim 2-3$ GeV, so the MB rate is a good approximation in the intermediate mass region when the net baryon density is small. However, at finite chemical potential, the MB approximation requires that $e^{(E_i-\mu_i)/T} >> 1$, so the condition becomes $E_i - \mu_i >> T$. Consequently, the larger μ_B becomes, the larger M must be for the FD rate to approach the MB result. At $\mu_B = 4T$, for example, the FD result does not converge to the MB approximation until $M > 5$ GeV. Therefore the Fermi-Dirac rates are necessary when probing the finite μ_B region of the QCD phase diagram.

It should be noted that all of these rates are defined in the local rest frame of the fluid. To make predictions of the total thermal dilepton yield measured in HIC experiments, one must perform a boost into the lab frame[1] prior to integrating over the momentum space. For the remainder of this thesis I will focus on the fully differential rate dR/d^4P in the local rest frame.

---

[1] Note that, in experiments with two colliding beams of equal energies, the lab frame is also the centre of mass frame of the collision.

Chapter 3

Dilepton Rates: NLO Contributions at Finite Baryon Density

3.1 Rates from Field Theory

Field theory provides another approach to formulating the thermal dilepton emission rate using the self-energy, $\Pi_{\mu\nu}$, of the virtual photon [43,46]. At 1-loop order, the self-energy is represented by the diagram in Figure 3.1. Higher order corrections to the self-energy are discussed in Section 3.1.3.

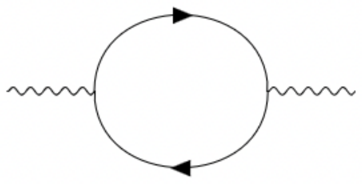

Figure 3.1: 1-loop Feynman diagram for the photon self-energy. Solid lines represent fermions and wavy lines represent photons.

The imaginary part of the photon self-energy, obtained by cutting the loop diagrams [46], defines the spectral function

$$\rho_{\mu\nu} = \mathrm{Im}[\Pi_{\mu\nu}]. \tag{3.1}$$

The differential rate with respect to the four-momentum $P_{\pm}$ of the outgoing dileptons can then be calculated from [2,43,46]:

$$E_{+}E_{-}\frac{dR}{d^3P_{+}d^3P_{-}} = \frac{n_B(E)}{2\pi^4 M^4}\left(\alpha_{em}^2 \sum_f e_f^2\right) B\left(\frac{m_l^2}{M^2}\right) L^{\mu\nu}\rho_{\mu\nu}. \tag{3.2}$$

As in Section 2.1, e_f^2 is the squared quark charge fraction which is summed over all quark flavours. Again, I will assume three quark flavours: up, down, and strange. The kinematic factor is defined as $B(x) = (1 + 2x)\Theta(1 - 4x)\sqrt{1 - 4x}$, and the tensor $L^{\mu\nu} = P_{+}^{\mu}P_{-}^{\nu} + P_{+}^{\nu}P_{-}^{\mu} - g^{\mu\nu}(P_{+} \cdot P_{-} + m_l^2)$ describes the coupling of the dileptons to the mediating photon. The momentum distribution of the photon is described by the Bose-Einstein distribution function $n_B(E) = \frac{1}{e^{E/T}-1}$, where $E = E_{+} + E_{-}$.

3.1.1 Polarized Dilepton Emission

The virtual photon spectral function, $\rho^{\mu\nu}$, can be decomposed into longitudinal and transverse components

$$\rho_{\mu\nu} = \mathbb{P}^{L}_{\mu\nu}\rho_{L} + \mathbb{P}^{T}_{\mu\nu}\rho_{T}, \tag{3.3}$$

using the longitudinal and transverse projection operators [47],

$$\mathbb{P}^L = \frac{1}{P^2}\begin{pmatrix} \mathbf{p}^2 & E|\mathbf{p}| \\ E|\mathbf{p}| & E^2\hat{p}_i\hat{p}_j \end{pmatrix}, \; \mathbb{P}^T = \begin{pmatrix} 0 & 0 \\ 0 & \delta_{ij} - \hat{p}_i\hat{p}_j \end{pmatrix}, \tag{3.4}$$

where $i, j = 1, 2, 3$ are the spacial indices and the unit momentum vectors are defined as $\hat{p}_i = \frac{\mathbf{p}_i}{|\mathbf{p}_i|}$. These projectors give the corresponding polarized spectral functions:

$$\begin{aligned} \rho_L &= \frac{P^2}{p^2}\rho_{00} \\ \rho_T &= \frac{1}{2}\left(\rho^\mu_\mu + \frac{P^2}{p^2}\rho_{00}\right). \end{aligned} \tag{3.5}$$

Now, using Eq. (3.3) and (3.4) in (3.2), summing over the quark flavours, and integrating over the allowed momentum-space of one of the dilepton products gives the more familiar dR/d^4P form of the dilepton rate derived in [3]:

$$\frac{dR}{d^4P} = \frac{dR}{dEd^3p} = \frac{2\alpha_{em}^2 n_B(E)}{9\pi^3 M^2} B\left(\frac{m_l^2}{M^2}\right)(2\rho_T + \rho_L). \tag{3.6}$$

3.1.2 LO Spectral Functions

At leading order in α_s, the photon self-energy is represented by the 1-loop diagram in Figure 3.1. The spectral function $\rho_V = \rho^\mu_\mu$ is directly related to the LO rate [46, 47] which was calculated at finite μ_B in [45]. A more general form[1] for both ρ_V and ρ_{00} at $\mu_B = 0$ is given in [41]. This has been extended to finite baryon density in [1] and [2], so the 1-loop

---

[1] These results also allow for $M^2 < 0$. A more detailed history of calculations in various kinematic limits is discussed in [41].

spectral functions are

$$\rho_V|_{1-loop} = -\frac{N_c M^2}{4\pi p}\left[T\sum_{\nu=\pm\mu}\left(l_1 f(p_+ - \nu) - l_1 f(|p_-| - \nu)\right) + p\theta(p_-)\right] \tag{3.7}$$

$$\begin{aligned}\rho_{00}|_{1-loop} = \quad & -\frac{N_c}{12\pi p}\left[12T^3\sum_{\nu=\pm\mu}\left(l_3 f(p_+ - \nu) - l_3 f(|p_-| - \nu)\right)\right. \\ & \left. + 6pT^2\sum_{\nu=\pm\mu}\left(l_2 f(p_+ - \nu) + \text{sign}(p_-) l_2 f(|p_-| - \nu)\right) + p^3\theta(p_-)\right].\end{aligned} \tag{3.8}$$

Equations (3.7) and (3.8) use $p_\pm = \frac{E\pm p}{2}$ as well as the following polylogarithms, defined in [2]:

$$l_{1f}(x) = \ln\left(1 + e^{-x/T}\right), l_{2f}(x) = \text{Li}_2\left(-e^{-x/T}\right), l_{3f}(x) = \text{Li}_3\left(-e^{-x/T}\right). \tag{3.9}$$

3.1.3 NLO Spectral Functions

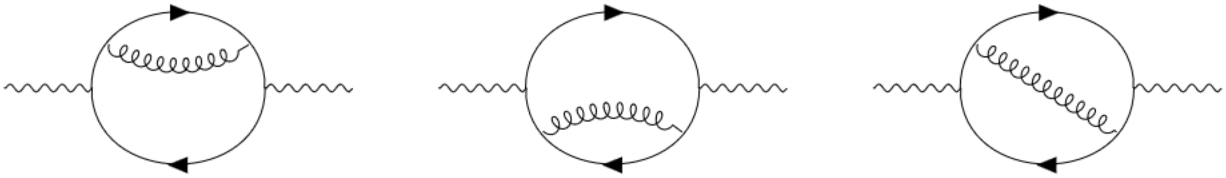

Figure 3.2: 2-loop Feynman diagrams for the photon self-energy. Solid lines represent fermions, wavy lines are photons, and curly lines are gluons.

NLO corrections to the spectral functions have been calculated at $\mu_B = 0$ [40] and at finite μ_B [1,2] by evaluating the 2-loop diagrams for the photon self-energy shown in Figure 3.2. The 2-loop spectral functions at finite μ_B are given by equations (11) and (12) in [2], where the authors have defined the results as a linear combination of integrals of the form:

$$\rho^{m,n}_{abcde}(P) = \text{Im}\left[\sum\!\!\!\!\!\!\int_{K,Q} \frac{k_0^m q_0^n}{[K^2]^a[Q^2]^b[(P-K-Q)^2]^c[(P-K)^2]^d[(P-Q)^2]^e}\right]. \quad (3.10)$$

P is the four-momentum of the photon and K and Q are the four-momenta of the pair of fermions[2]. The 2-loop spectral functions in [2] also depend on the strong coupling α_s, unlike the 1-loop terms[3].

For $M > T$, the full NLO spectral functions, ρ_i, where $i = T, L, V,$ or 00, can simply be calculated from the sum of the 1-loop and 2-loop diagrams:

$$\rho_i|_{NLO} = \rho_i|^{strict}_{1-loop} + \rho_i|^{strict}_{2-loop}. \quad (3.12)$$

However, Landau–Pomeranchuk–Migdal (LPM) resummation [48] is needed to handle singularities that appear in certain cases of Eq. (3.10) as $M \to 0$ [1]. The full LPM calculations in [48] already include approximations of the 1-loop and 2-loop terms that are only valid in the small M limit. The process of re-expanding the LPM results to eliminate this double counting is described in [1, 2]. So now, the general NLO result for all M, is

---

[2] In $D = d + 1 = 4 - 2\epsilon$ spacetime dimensions, the sum-integral notation, adopted from [1,2], is

$$\sum\!\!\!\!\!\!\int_P = \int_{\mathbf{p}} T \sum_{p_0} \text{ and } \int_{\mathbf{p}} = \left(\frac{e^{\gamma}\bar{\mu}^2}{4\pi}\right)^{\epsilon} \int \frac{d^d p}{(2\pi)^d}. \quad (3.11)$$

[3] Equations (11) and (12) in reference [2] are written in terms of g which is related to $\alpha_s = g^2/(4\pi)$.

obtained from

$$\rho_i|_{NLO} = \rho_i|^{strict}_{1-loop} + \rho_i|^{strict}_{2-loop} + \rho_i|^{full}_{LPM} - \rho_i|^{expanded}_{LPM}, \tag{3.13}$$

where $\rho_i|^{expanded}_{LPM}$ contains the extra 1-loop and 2-loop terms that need to be removed from $\rho_i|^{full}_{LPM}$ [2].

3.2 Comparing LO and NLO Rates at Zero Baryon Density

Assuming zero baryon chemical potential for now, I explore the effect of the NLO contributions on dilepton production with respect to the invariant mass and momentum of the lepton pair. In the following analysis, I use the full NLO spectral functions, including the LPM effect, from [2][4]. The full LO spectral functions are obtained from the NLO case by setting $\alpha_s = 0$. I will assume mid-rapidity so that $p = p_T$.

In general, the dilepton rate is also dependent on the temperature of the plasma. Under the assumption of massless leptons ($m_l = 0$), the temperature dependence of dR/d^4P can be absorbed by replacing invariant mass, transverse momentum, and baryon potential with the temperature scaled variables:

$$\begin{aligned} M &\to \frac{M}{T} \\ p_T &\to \frac{p_T}{T} \\ \mu_B &\to \frac{\mu_B}{T}. \end{aligned} \tag{3.14}$$

---

[4] Greg Jackson contributed the numerical table and interpolation for the full LO and NLO spectral functions used in Chapters 3 and 4 of this thesis.

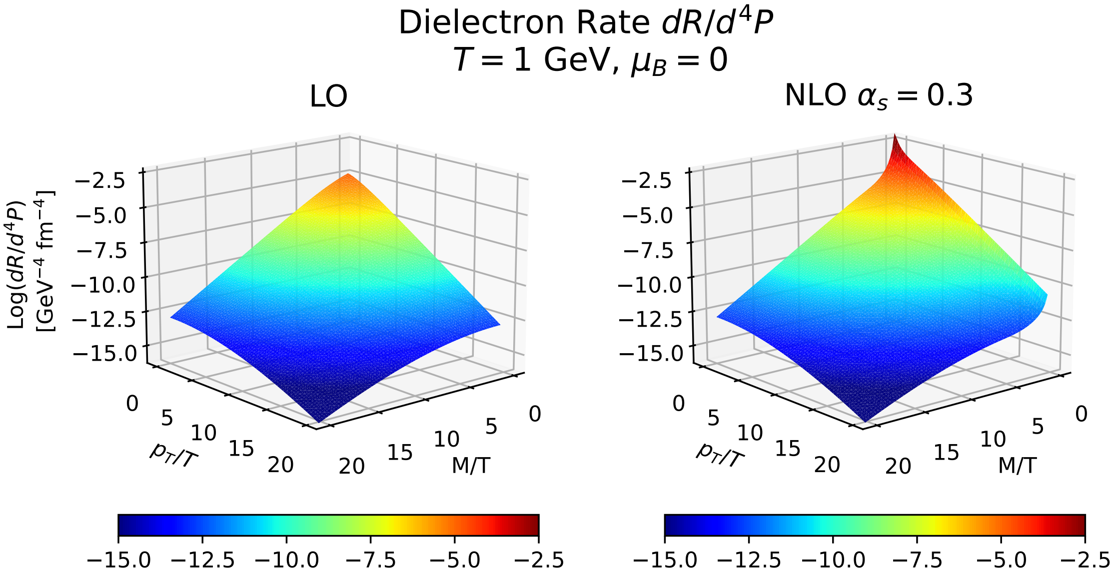

Figure 3.3: Comparison of mid-rapidity (y=0) dielectron rate at LO (left) and NLO (right) with respect to M/T and p_T/T. The NLO results use a fixed coupling of $\alpha_s = 0.3$. The colourbars use the same logarithmic scale as the vertical axis.

However, the full LO and NLO rates used here are calculated from Eq. (3.6), which does include the lepton mass. Rewriting Eq. (3.6) with the change of variables above gives

$$\frac{dR}{d^4P} = \frac{2\alpha_{em}^2 n_B(E)}{9\pi^3 (M/T)^2} B\left(\frac{m_l^2/T^2}{(M/T)^2}\right)\frac{1}{T^2}\left[2\rho_T\left(\frac{M}{T},\frac{p_T}{T},\frac{\mu_B}{T}\right) + \rho_L\left(\frac{M}{T},\frac{p_T}{T},\frac{\mu_B}{T}\right)\right]. \quad (3.15)$$

The spectral functions $\rho_i\left(\frac{M}{T},\frac{p_T}{T},\frac{\mu_B}{T}\right)$ each carry an overall factor of T^2 which will cancel with the factor of $1/T^2$ in Eq. (3.15). Therefore, the only source of explicit temperature dependence is the kinetic factor $B\left(\frac{m_l^2/T^2}{(M/T)^2}\right)$. In the case of dielectron production, the effect of varying temperature will be very small except near $M \lesssim m_e$. Thus, for convenience, I will set $T = 1$ GeV.

Figure 3.3 shows the differential rate dR/d^4P at mid-rapidity as a 3D surface with respect to M/T and p_T/T. LO results are shown on the left, and the full NLO rate, with

$\alpha_s = 0.3$, is shown on the right, with the same logarithmic axis used for both. The fixed coupling of $\alpha_s = 0.3$ has been chosen for consistency with other heavy-ion studies, as discussed in [49]. Both the LO and NLO rates are large when M and p_T are small relative to the temperature of the plasma. The rates decrease as M/T and p_T/T increase. The effect of the NLO terms is most obvious at low M/T for all values of p_T/T, which is consistent with [3]. The LO rate reaches a maximum of $\sim 10^{-5}$ GeV^{-4}fm^{-4} as M/T and $p_T/T \to 0$. At this point the NLO contributions enhance the rate by approximately 2 orders of magnitude. This enhancement is attributed to the bremsstrahlung processes that are included only in the 2-loop self-energy diagrams, in addition to corrections to the $q\bar{q} \to \ell^-\ell^+$ diagram [43]. Bremsstrahlung dileptons are expected to dominate at low M, where the enhancement is greatest.

The effect of varying the QCD coupling constant is demonstrated in Figure 3.4, which shows dR/d^4P versus p_T/T for fixed values of $M/T = 1, 5, 7.5$, and 10. From this perspective, it is easier to quantitatively compare the effect of the NLO contributions to the LO results. In general, the rate is enhanced at NLO, and as expected, increasing α_s increases the difference between the LO and NLO rates. It is also clear that the effect is most significant at low M/T. In the $M/T = 1$ case, a coupling strength of $\alpha_s = 0.3$ increases the rate by about one order of magnitude compared to the pure LO rate. For $\alpha_s = 0.05$ and 0.1 the rate approximately increases by a factor of 2 and 3 respectively. Beyond $M/T = 5$ there is very little effect for $\alpha_s = 0.05$ and 0.1, and the $\alpha_s = 0.3$ result is less than 1.5 times larger.

Although I will focus on the thermal contribution in this work, the total dilepton yield over the entire collision should include contributions from the pre-equilibrium and hadronic stages in order to compare with experimental measurements. In particular, the

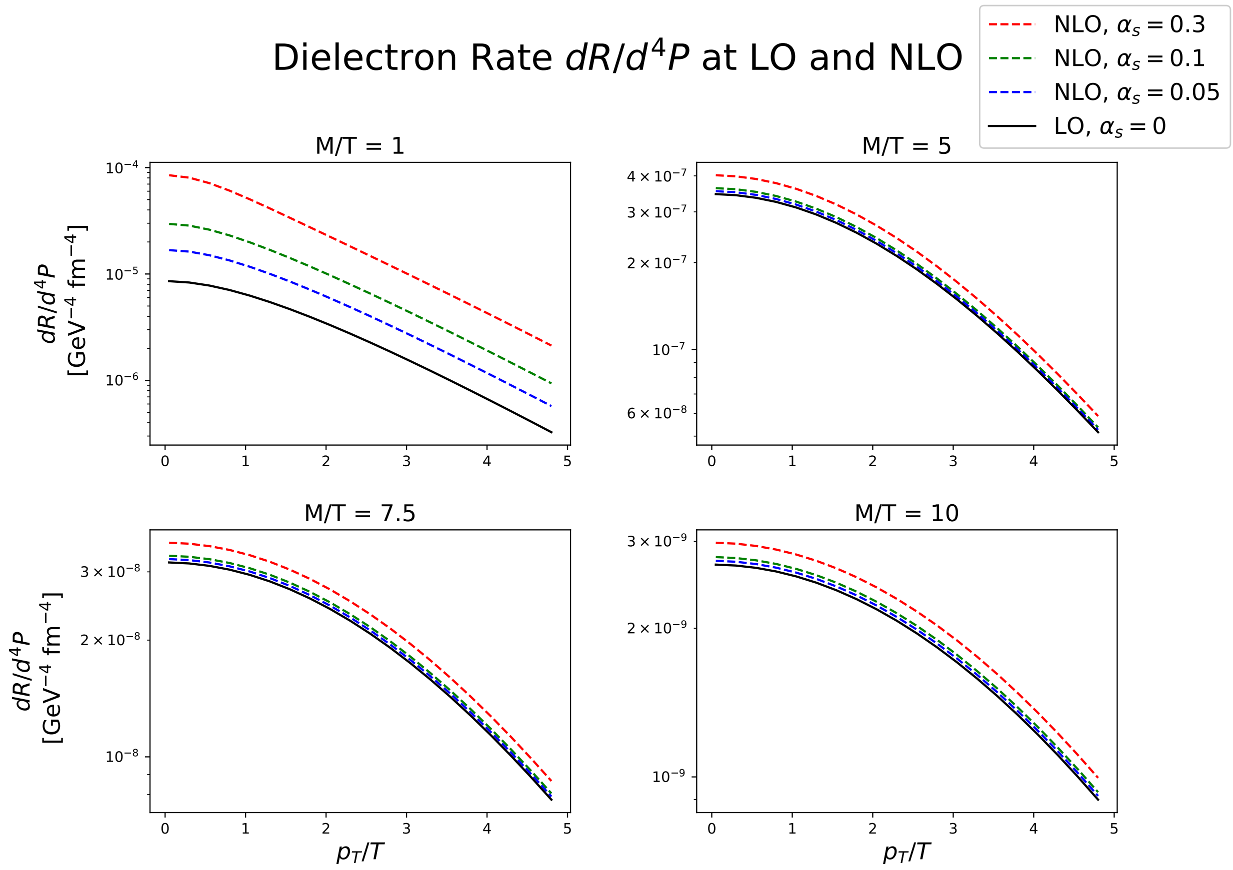

Figure 3.4: Effect of α_s on the p_T/T spectrum of dR/d^4P at mid-rapidity. Full LO (solid black) and NLO results with fixed coupling $\alpha_s = 0.05, 0.1,$ and 0.3 (dashed blue, green, and red) are shown at $M/T = 1, 5, 7.5$ and 10.

hadronic stage dominates in the low mass domain, where $M < 1$ GeV [38]. However, at intermediate masses, $M \sim 1 - 3$ GeV, the thermal QGP dilepton spectrum is cleaner. As such, the following results and discussion are most useful for $M > 1$ GeV. For the temperature-scaled parameters used here, the intermediate mass region depends on the choice of T. So for example, at a typical temperature of $T = 0.4$ GeV, the intermediate mass region begins at $M/T > 2.5$.

3.3 Effect of Finite Baryon Density on NLO Rates

Now the effect of finite baryon density can be compared at LO and NLO for the differential rates discussed in the previous section. Four values of finite μ_B/T are used to compare to the zero net baryon density case. The smallest three values, $\mu_B/T = 1.2, 1.9$, and 3.5, are the respective minimum, average, and maximum values extracted from the 20-30% centrality bin of hydrodynamic simulations[5] for Au-Au collisions at 7.7 GeV. For comparison, increasing the collision energy to 19.6 GeV reduces these values to $\mu_B/T = 0.005, 1.1$, and 2.5, so the effect of μ_B on the rates should be more apparent in lower energy collisions. One additional value of $\mu_B/T = 6$ is selected to consider the effect of further increasing the baryon asymmetry beyond what is expected from the hydro simulations. It is possible that even lower energy collisions with larger net baryon density may be needed to produce a measurable effect.

Figure 3.5 shows the effect of μ_B/T on the p_T/T spectrum of dR/d^4P at fixed values of M/T. LO results (solid) are compared to the full NLO rates (dashed) with QCD coupling $\alpha_s = 0.3$. The same values of M/T are used as in Figure 3.4.

At LO, the rate is suppressed by μ_B, as demonstrated in [45]. The suppression is greatest in the $M/T = 1$ case for $p_T/T \to 0$, and decreases as either variable is increased. This behaviour is expected, given that μ always appears in the rate in the form exp$(\frac{|E \pm p|}{2} - \mu)$, which behaves like exp$(\frac{|E \pm p|}{2})$ when both M and p are much larger than μ.

The most interesting result seen here is that, unlike at LO, the NLO rate is enhanced at $M/T = 1$. This is counter-intuitive, as increasing μ_B means that there will be a smaller

---

[5] (3+1)D MUSIC results were provided by Lipei Du. The framework for the evolution is outlined in [50].

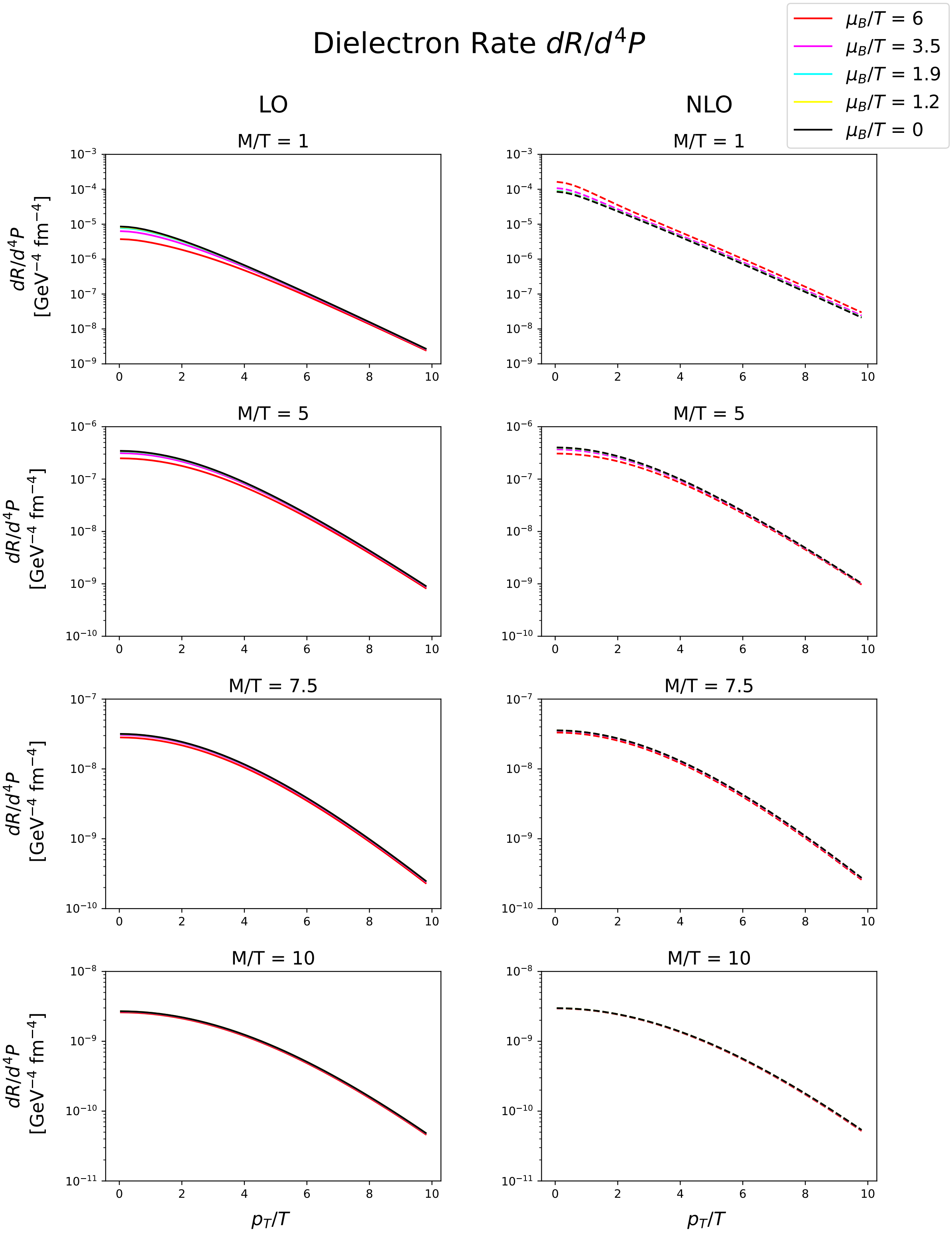

Figure 3.5: Effect of μ_B on the p_T spectrum of the mid-rapidity dielectron rate, $\frac{dR}{d^4P}$, at fixed values of M/T. LO results (solid) are shown on the left, and NLO (dashed) with $\alpha_s = 0.3$ are on the right. From top to bottom the invariant mass values are $M/T = 1, 5, 7.5$, and 10.

proportion of quark-antiquark pairs available to interact. However, as mentioned, the NLO corrections contain bremsstrahlung terms that dominate at low M. These interactions do not require pairs of quarks and antiquarks. So while increasing μ_B reduces the rate of $q\bar{q}$ annihilation, the bremsstrahlung rate is increased. In the case of thermal photons, it was shown that the enhancement of the quark bremsstrahlung at finite μ_B is stronger than the suppression of the $q\bar{q}$ annihilation [51]. Notably, the enhancement seen in the rates here was not observed in [3], where it was concluded that μ_B did not have a significant effect on the p_T integrated yields. Recall that for 7.7 GeV, hydrodynamic models had an average of $\mu_B = 1.9$, which has a very small effect in Figure 3.5. This highlights the need for yield predictions at even lower energies.

As M increases, the NLO rate becomes suppressed by μ_B, as in the pure LO case. This can be seen at $M/T = 5, 7.5$, and 10 in Figure 3.5. Recall from Section 3.2 that the NLO contributions become small for $M/T \gtrsim 5$, which can explain the transition from enhancement to suppression as M increases. This transition is shown more clearly in Figure 3.6. First, however, it is important to note that the overall magnitude of the μ_B effect is small relative to the NLO contributions. This is particularly true at $M/T = 1$, where the LO and NLO rates at $\mu_B/T = 0$ differ by an order of magnitude. In comparison, $\mu_B/T = 6$ changes the LO and NLO rates by a factor of $\lesssim 2$.

Figure 3.6 shows the percent difference between the rate at finite μ_B/T and at zero baryon density:

$$\frac{|dR/d^4P(\mu_B) - dR/d^4P(0)|}{dR/d^4P(0)} * 100\%. \tag{3.16}$$

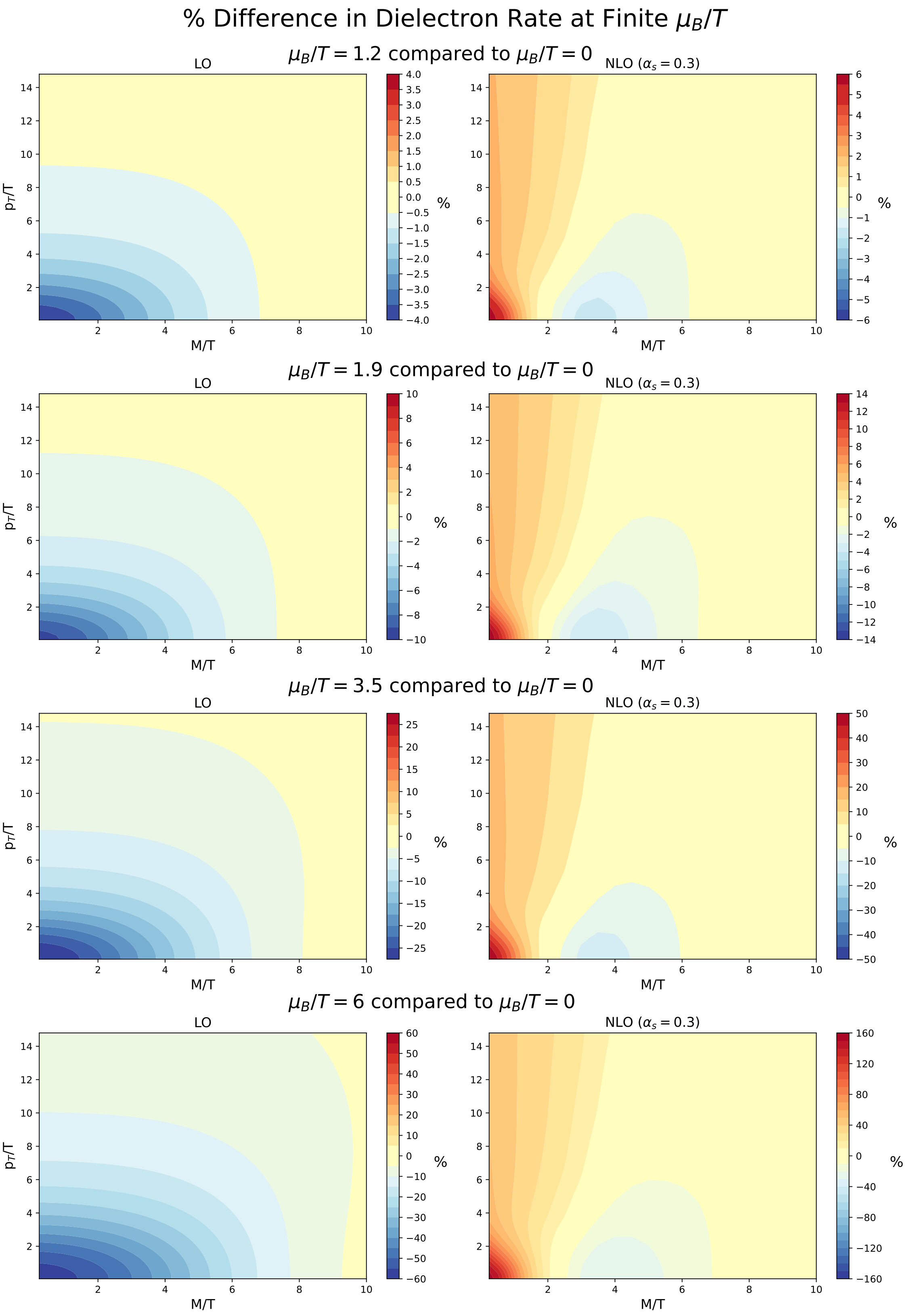

Figure 3.6: 2D contour plots of the percent difference in dR/d^4P at finite μ_B relative to $\mu_B = 0$. LO results (left) and NLO results at $\alpha_s = 0.3$ (right) are shown for $\mu_B/T = 1.2$, 1.9, 3.5, and 6.

2D contour plots are used to highlight the M/T and p_T/T dependence of the finite μ_B effect and compare the differences in structure at LO and NLO.

At LO (left), the rate is maximally suppressed as $M/T \to 0$ and $p_T/T \to 0$. The suppression decreases towards larger M/T and p_T/T and eventually disappears. At NLO, the rate is maximally enhanced rather than suppressed at small M/T and p_T/T. Furthermore, the μ_B effect does not disappear at large p_T/T as observed in the LO case. Increasing M/T reduces the strength of the enhancement until the effect reverses and the rate is suppressed at intermediate M/T. At $p_T/T \approx 0$, the transition from enhancement to suppression occurs around $M/T \approx 2$. The transition point shifts towards larger M/T as p_T/T increases. The maximum suppression occurs at low p_T/T around $M/T = 3 - 4$. After this point, the effect of μ_B decreases and disappears towards large M/T.

Varying μ_B/T changes the strength of the suppression or enhancement, but not the general structure with respect to M/T and p_T/T. For $\mu_B/T = 1.9$, which was the average value extracted from the hydrodynamic simulations, the LO rate experiences a maximum suppression of $\sim 10\%$. At NLO, the maximum enhancement is slightly stronger at $\sim 14\%$. Increasing the baryon potential to $\mu_B/T = 3.5$ increases the effect to $\sim 25\%$ and 50% respectively for LO and NLO, and at $\mu_B/T = 6$ these values become $\sim 60\%$ and 160%.

Overall, the NLO contributions to the dilepton rate are more significant than the finite μ_B effect. However, the effect of μ_B is non-negligible at larger values ($\mu_B/T \sim 6$), which is promising for future investigation of dilepton yields in lower energy experiments. Furthermore, the full NLO rates are more strongly affected by μ_B compared to the LO rates.

Chapter 4

Dilepton Rates: Polarization

In this chapter, I analyze the effect of NLO contributions and finite baryon density in the context of the virtual photon polarization. Recall from Section 3.1.1, the total rate can be decomposed into two components, which depend on the transverse and longitudinal spectral functions ρ_T and ρ_L.

To characterize the relative amount of transverse and longitudinal polarization in the dilepton signal, I define the spectral function ratio

$$r_{TL} = \frac{\rho_T}{\rho_L}. \tag{4.1}$$

Another quantity frequently discussed in the literature is the fractional anisotropy

$$\lambda = \frac{\rho_T - \rho_L}{\rho_T + \rho_L}. \tag{4.2}$$

Here, a mostly transverse signal would have $\lambda > 0$, while mostly longitudinal would give $\lambda < 0$. The magnitude indicates the relative strength of the anisotropy. Purely transverse and purely longitudinal signals correspond respectively to the maximum and minimum values $\lambda = \pm 1$, and $\lambda = 0$ for the isotropic case where $\rho_T = \rho_L$.

4.1 Comparing Polarization at LO vs NLO

Figure 4.1 shows the M/T and p_T/T dependence of the spectral function ratio r_{TL} at LO and NLO with a QCD coupling strength of $\alpha_s = 0.05, 0.1,$ and 0.3. At LO only (top left), one can see that $r_{TL} \leq 1$ over the entire M/T and p_T/T grid. Therefore, it is always the case that $\rho_T \leq \rho_L$ at LO. The asymmetry in the polarization is greatest at very low mass and intermediate p_T/T where ρ_T is approximately 10% smaller than ρ_L.

Introduction of the NLO terms dramatically alters the polarization of the differential dilepton rate. Most notably, the polarization is completely inverted at low M so that the transverse component dominates. Even for a QCD coupling strength of only $\alpha_s = 0.05$, ρ_T becomes as great as 40 times larger than ρ_L at small M/T and large p_T/T. Increasing α_s to 0.1 and 0.3 has little effect on the general structure of the NLO polarization ratio, aside from further enhancing r_{TL} at low M/T.

Figure 4.2 provides a better view of the small scale variation in NLO r_{TL} by cutting out the low M region. This reveals structure similar to what is seen at leading order. In addition to enhancing the ratio at low M, increasing α_s also shifts the location of the minimum r_{TL} towards larger M/T.

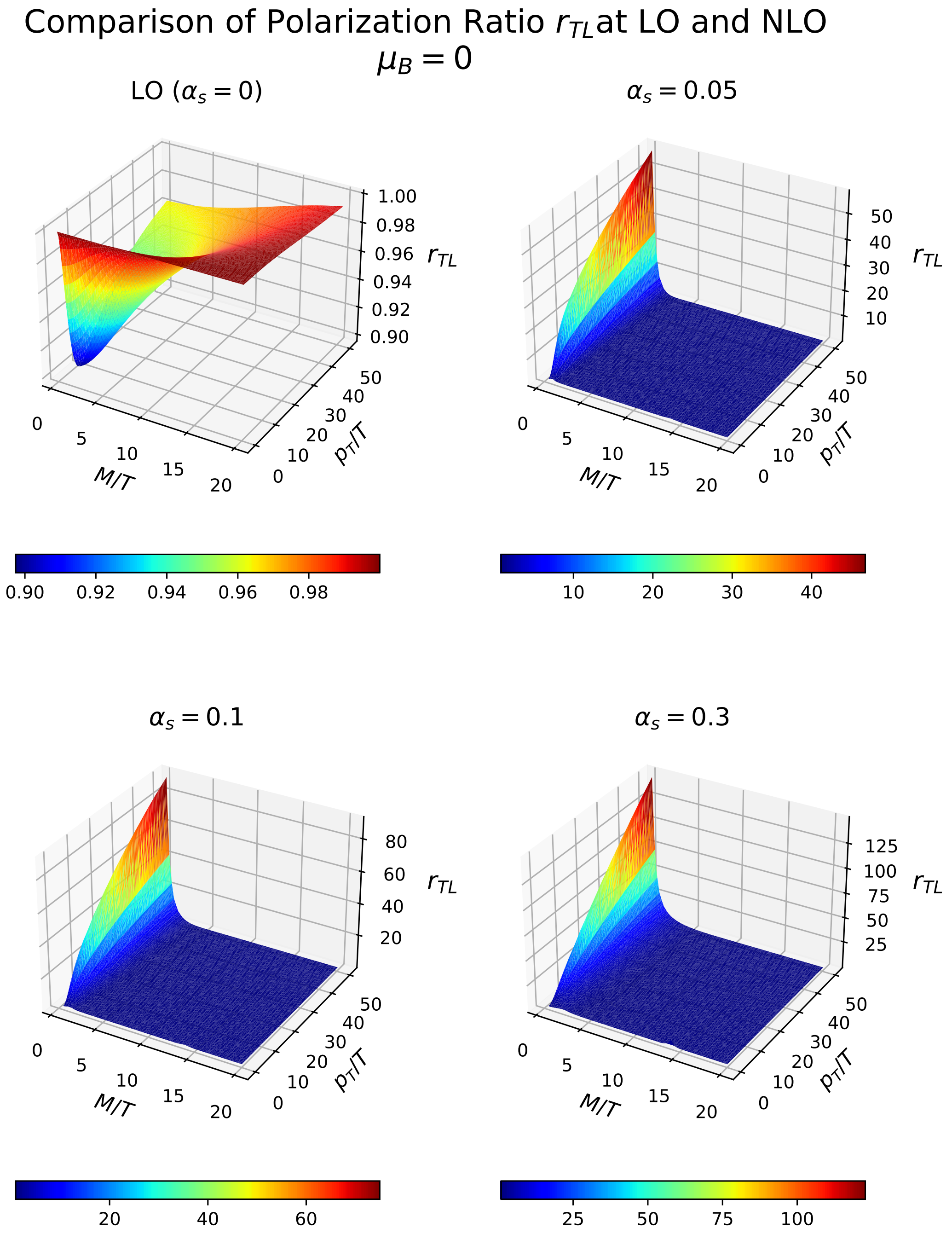

Figure 4.1: Polarization ratio, ρ_T/ρ_L, shown at LO (top left) and NLO with $\alpha_s = 0.05$, 0.1, and 0.3 (top right, lower left, and lower right respectively). Results are shown over the region $M/T : [0, 20]$ and $p_T/T : [0, 40]$.

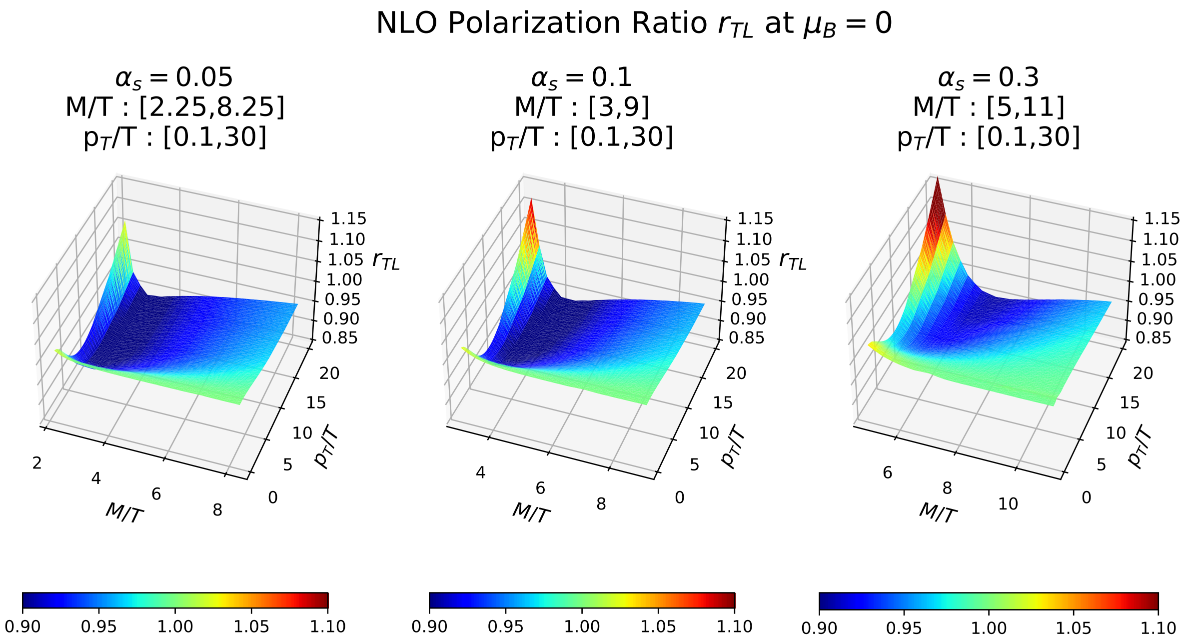

Figure 4.2: NLO polarization ratio, ρ_T/ρ_L, shown over different ranges of M/T and p_T/T, to reveal the small scale structure. (a) $\alpha_s = 0.05$ on $M/T : [2.25, 8.25]$ and $p_T/T : [0.1, 30]$, for , (b) $\alpha_s = 0.1$ on $M/T : [3, 9]$ and $p_T/T : [0.1, 30]$, (c) $\alpha_s = 0.3$ on $M/T : [5, 11]$ and $p_T/T : [0.1, 30]$.

4.2 Effect of Finite Baryon Chemical Potential

The following section investigates the effect of baryon chemical potential μ_B on the dilepton polarization at LO and NLO. Realistic values of finite μ_B/T were selected based on the results of relativistic hydrodynamic simulations[1] as described in Section 3.3.

Figure 4.3 shows the finite μ_B results for the spectral function ratio, r_{TL}, with respect to p_T/T at fixed values of M/T. From top to bottom the rows display results with $M/T = 1, 5, 7.5$ and 10 at both LO (solid lines) and NLO (dashed lines). The NLO results here include the 1-loop, 2-loop, and corrected LPM contributions from [2]. As in Chapter 3, I

---

[1] (3+1)D MUSIC results were provided by Lipei Du. The framework for the evolution is outlined in [50].

use $\alpha_s = 0.3$ for the QCD coupling strength. Figures 4.4 - 4.6 are the analogous results for λ and the individual spectral functions, ρ_T and ρ_L. However, the following discussion will focus mostly on the r_{TL} results.

4.2.1 Polarization at Zero Chemical Potential

The general M/T and p_T/T dependence of r_{TL} at zero baryon density was briefly discussed in the previous section. Figure 4.3 can now be used to discuss the $\mu_B/T = 0$ case in more quantitative detail.

First, note that the LO results for $\mu_B/T = 0$ (solid black curve) confirm that $r_{TL} \leq 1$ at LO as observed previously in Figure 4.1. We also see that $r_{TL} \to 1$ near $p_T = 0$ as expected, since the longitudinal and transverse spectral functions should be equal at $p_T = 0$. The general p_T/T dependence at LO is similar for each value of M/T shown in Figure 4.3. As p_T/T increases, r_{TL} decreases until reaching a minimum at intermediate p_T/T. After this point r_{TL} gradually increases again; however, the longitudinal polarization remains dominant. At $M/T = 1$ the polarization ratio reaches a minimum value of $r_{TL} = 0.9$, indicating that ρ_T is 10% smaller than ρ_L, at $p_T/T \approx 8$. As M/T increases, the minimum shifts towards greater p_T/T. Simultaneously, the amount by which the minimum deviates from $r_{TL} = 1$ decreases. For $M/T = 10$ the minimum occurs at $p_T/T \approx 25$, where $r_{TL} = 0.97$. Evidently, the longitudinal component is only marginally larger than the transverse component in the LO rates.

In contrast, the NLO results in Figure 4.3 show much more variation in the strength of the polarization and dependence on M/T and p_T/T. Here, the transverse component

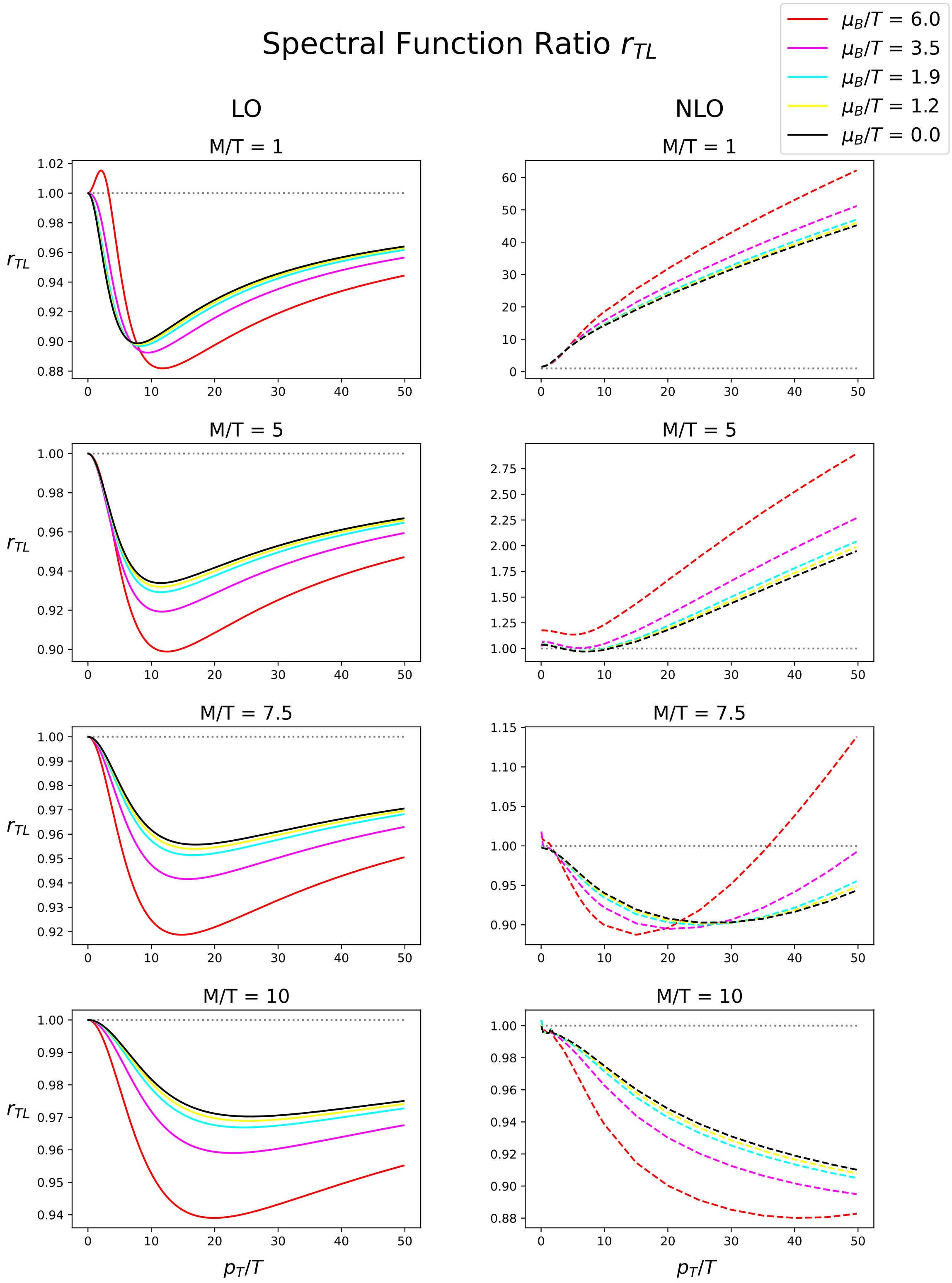

Figure 4.3: The effect of μ_B on the polarization ratio, $r_{TL} = \rho_T/\rho_L$, is shown with respect to p_T/T, at fixed values of $M/T = 1, 5, 7.5$, and 10 (from top to bottom). LO results (solid) are shown on the left, and NLO (dashed) with $\alpha_s = 0.3$ are on the right.

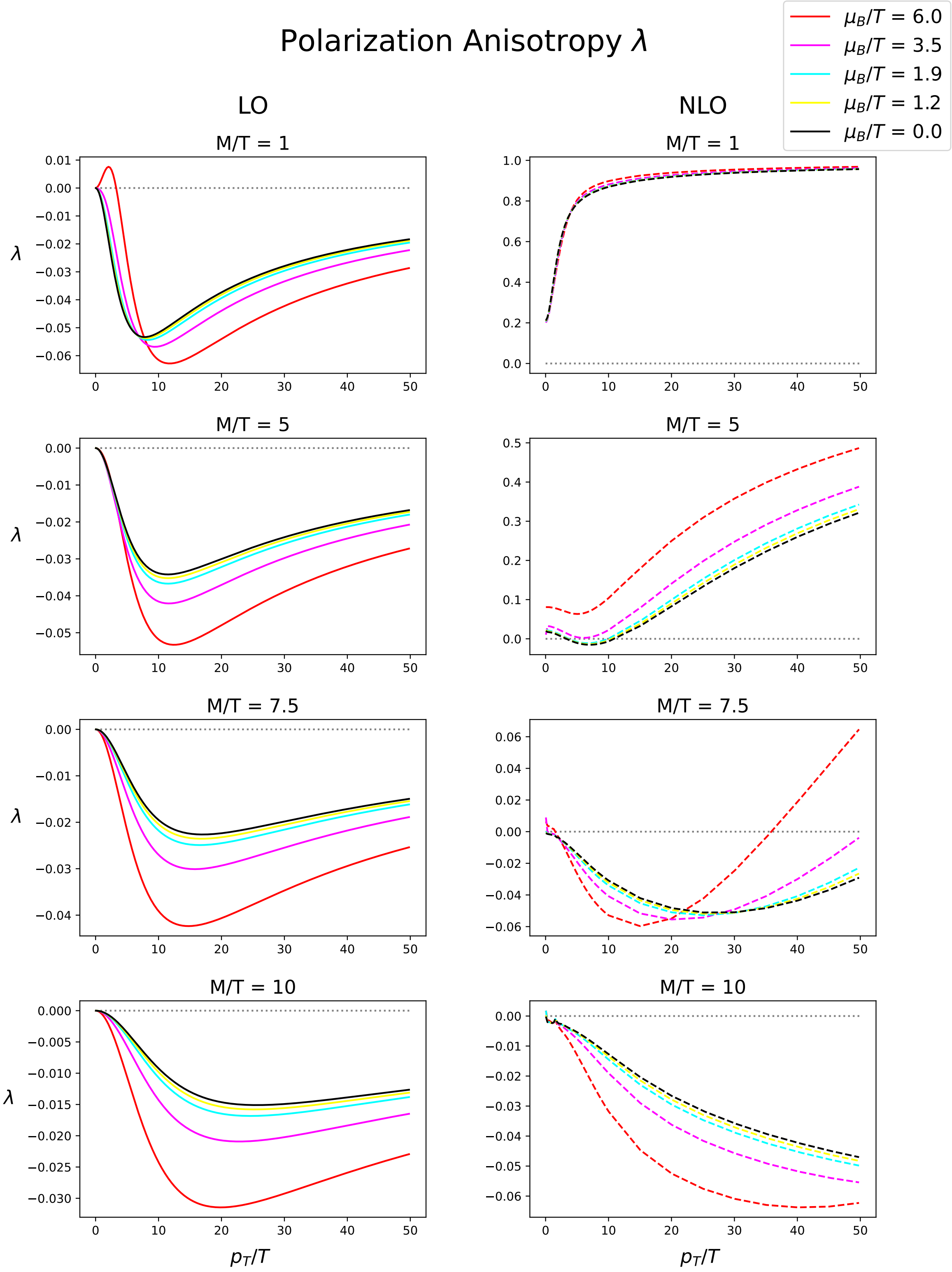

Figure 4.4: The effect of μ_B on the polarization anisotropy, λ, is shown with respect to p_T/T, at fixed values of $M/T = 1, 5, 7.5$, and 10 (from top to bottom). LO results (solid) are shown on the left, and NLO (dashed) with $\alpha_s = 0.3$ are on the right.

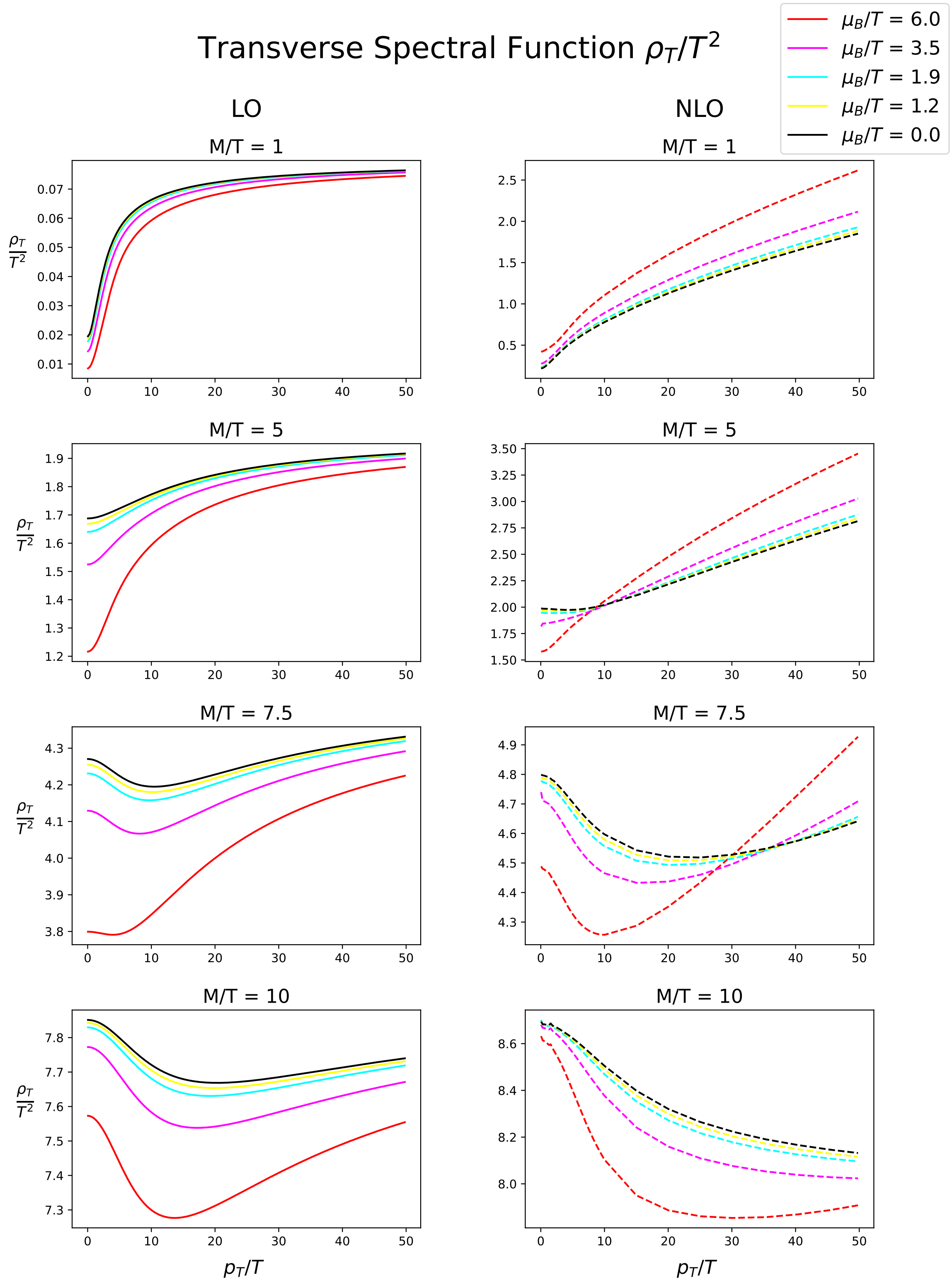

Figure 4.5: The effect of μ_B on the transverse polarization is shown with respect to p_T/T, at fixed values of $M/T = 1, 5, 7.5$, and 10 (from top to bottom). LO results (solid) are shown on the left, and NLO (dashed) with $\alpha_s = 0.3$ are on the right.

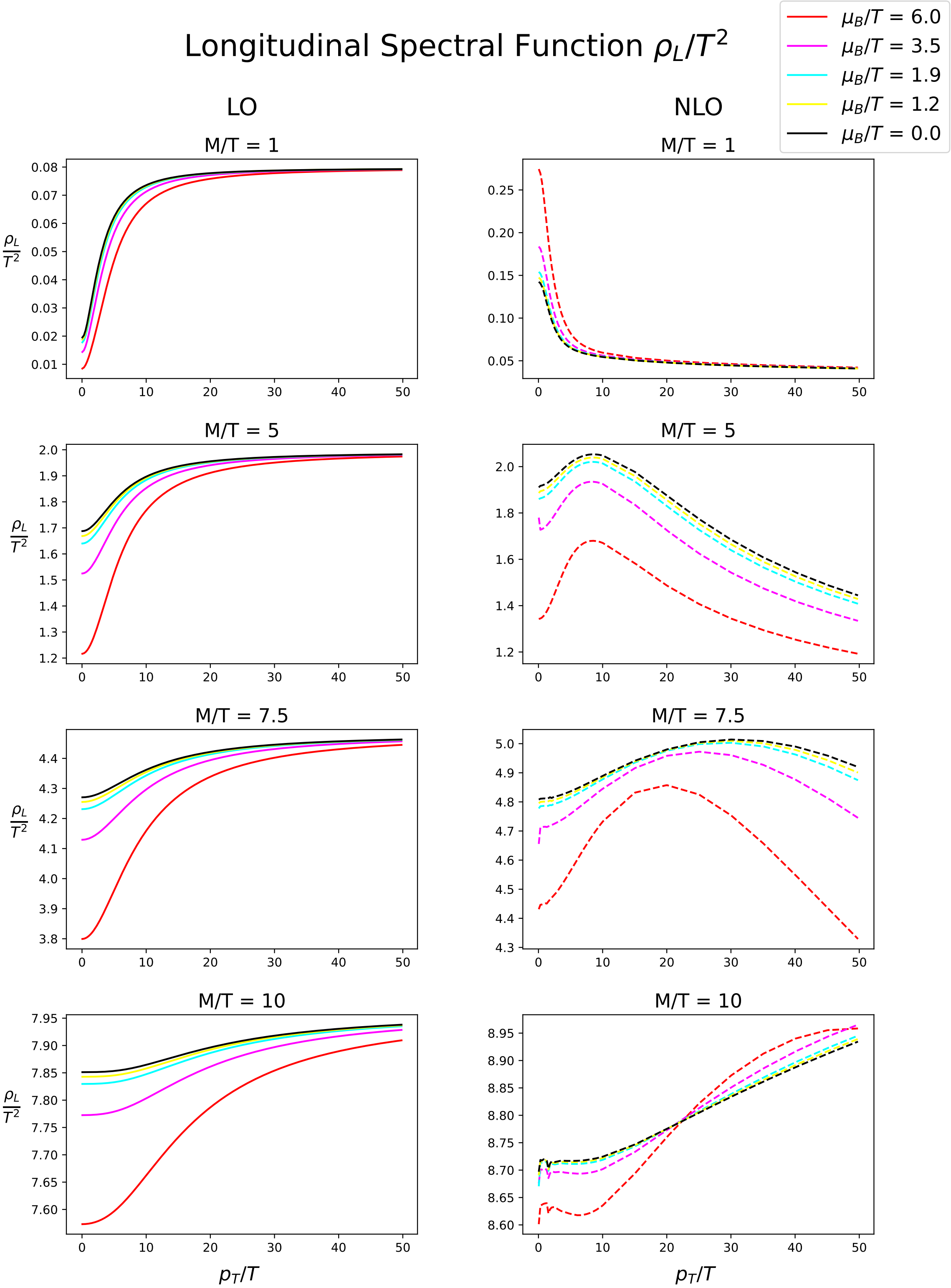

Figure 4.6: The effect of μ_B on the longitudinal polarization is shown with respect to p_T/T, at fixed values of $M/T = 1, 5, 7.5$, and 10 (from top to bottom). LO results (solid) are shown on the left, and NLO (dashed) with $\alpha_s = 0.3$ are on the right.

completely dominates in the region of low M/T, and intermediate to high p_T/T. Most notably, at $M/T = 1$, we see that $r_{TL} > 1$ over the entire p_T/T range and increases with p_T/T. At $p_T/T = 50$ the transverse spectral function is more than 40 times greater than the longitudinal component.

At $M/T = 5$, the polarization is still mostly transverse, however, the ratio is much weaker than at lower M/T. For $p_T/T < 10$ the ratio is close to 1. The proportion of transverse polarization increases for $p_T/T > 10$, but only reaches $r_{TL} \approx 1.8$ at $p_T/T = 50$.

Between at $M/T = 5$ and 7.5 the polarization has switched to slightly favour the longitudinal component at zero baryon density. At $M/T = 7.5$ the ratio reaches a minimum of $r_{TL} \approx 0.92$ at $p_T/T \approx 15$. As invariant mass continues to increase, the minimum is shifted to $p_T/T > 50$ at $M/T = 10$.

It should be emphasized that these results constitute the first comparison of dilepton polarization at LO and NLO in HICs. Importantly, we see that the NLO corrections have a significant effect on the thermal dilepton polarization. Although this effect is strongest at low M/T, where hadronic dileptons are expected to dominate, the NLO polarizations continue to show much richer structure than the LO results in the intermediate mass region. Therefore, including NLO corrections will be essential for comparing predictions of polarized dilepton emission to future measurements and probing the underlying physics.

4.2.2 Polarization at Finite Baryon Potential

Now consider the finite $\mu_B/T = 1.2, 1.9, 3.5,$ and 6 (yellow, green, magenta, and red) results in Figure 4.3. Overall, $\mu_B/T = 1.2$ and 1.9 have a negligible effect at both LO and

NLO. In particular, at small M the contribution of the NLO terms is much more significant than the effect of μ_B. At $M/T = 1$ the r_{TL} is 1 to 2 orders of magnitude greater at NLO compared to LO.

At LO, r_{TL} is almost exclusively suppressed by the presence of finite μ_B, with the exception of a small region at low M and low p_T. In the $M/T = 1$ panel, the ratio is slightly enhanced relative to zero μ_B at $p_T/T \leq 8$. With a baryon potential of $\mu_B/T = 6$, this effect is large enough to produce $r_{TL} > 1$ for the momentum region $0 < p_T/T < 6$, which indicates that the transverse spectral function becomes larger than the longitudinal component in this small region. Figures 4.6 and 4.5 show that increasing μ_B suppresses both spectral functions at LO. Therefore, the suppression of ρ_L must be stronger than the effect on ρ_T at low M/T and p_T/T in order to enhance the polarization ratio.

At NLO, the presence of finite μ_B tends to increase r_{TL} at low M. This can be seen in Figure 4.3 at $M/T = 1$ and 5, where the polarization is already mostly transverse. When the dominant polarization switches from transverse to longitudinal at intermediate M/T, the effect of μ_B also begins to reverse. This reversal affects the lower p_T/T range first. This is shown at $M/T = 7.5$, where increasing μ_B suppresses r_{TL} at low p_T/T but still increases the ratio at higher p_T/T. Increasing μ_B/T also shifts this crossover point towards lower p_T/T. This shift is very small for $\mu_B/T = 1.2, 1.9,$ and 3.5, but between $\mu_B/T = 3.5$ and $\mu_B/T = 6$ the crossover is shifted from $p_T/T \approx 28$ to 22. At $M/T = 10$, the polarization ratio is suppressed for the entire p_T/T range shown.

To summarize, increasing μ_B generally enhances the anisotropy between the transverse and longitudinal polarization that is already present at zero baryon density. This was also true at purely LO, where the polarization was mostly longitudinal and became even more longitudinal as the baryon potential increased.

To quantify the strength of the μ_B effect, I calculate the percent difference between the polarization ratio at finite μ_B compared to zero μ_B. Figure 4.7 presents the percent difference in r_{TL} as a 2D contour map, which shows how the effect of μ_B varies over $0 < M/T < 20$ and $0 < p_T/T < 40$ at LO and NLO for each of the four μ_B values used previously.

I have noted already that r_{TL} is mostly suppressed at LO. It is also clear that changing the value of μ_B does not alter the general structure. Figure 4.7 shows that the maximum suppression occurs near $M/T = 6$ and $p_T/T = 12$. However, r_{TL} is enhanced for $M/T < 3$ and $p_T/T < 5$. This is maximized at very small invariant mass and $p_T/T \approx 2$.

For $\mu_B/T = 1.2$ and 1.9 the amount of enhancement or suppression of LO r_{TL} is always less than 1%. This only increases to about 2% for $\mu_B/T = 3.5$. However, if lower energy collisions can be used to produce a baryon potential of $\mu_B/T = 6$, this can achieve a maximum of 7-8% enhancement in r_{TL} and a maximum suppression of 3-4%.

On the other hand, at NLO, a similar degree of enhancement can be achieved with only $\mu_B/T = 1.9$, which is the average value seen in MUSIC simulations for Au-Au at 7.7 GeV and 20-30% centrality. Further increasing the baryon potential to $\mu_B/T = 6$ can increase r_{TL} by over 60%. At NLO the enhancement is maximized around $3 < M/T < 4$ and $p_T/T \approx 2.5$. The maximum suppression of r_{TL} is at small M/T and p_T/T. Interestingly, this is the region that was strongly enhanced at LO, and is also where the total dilepton production rate is greatest.

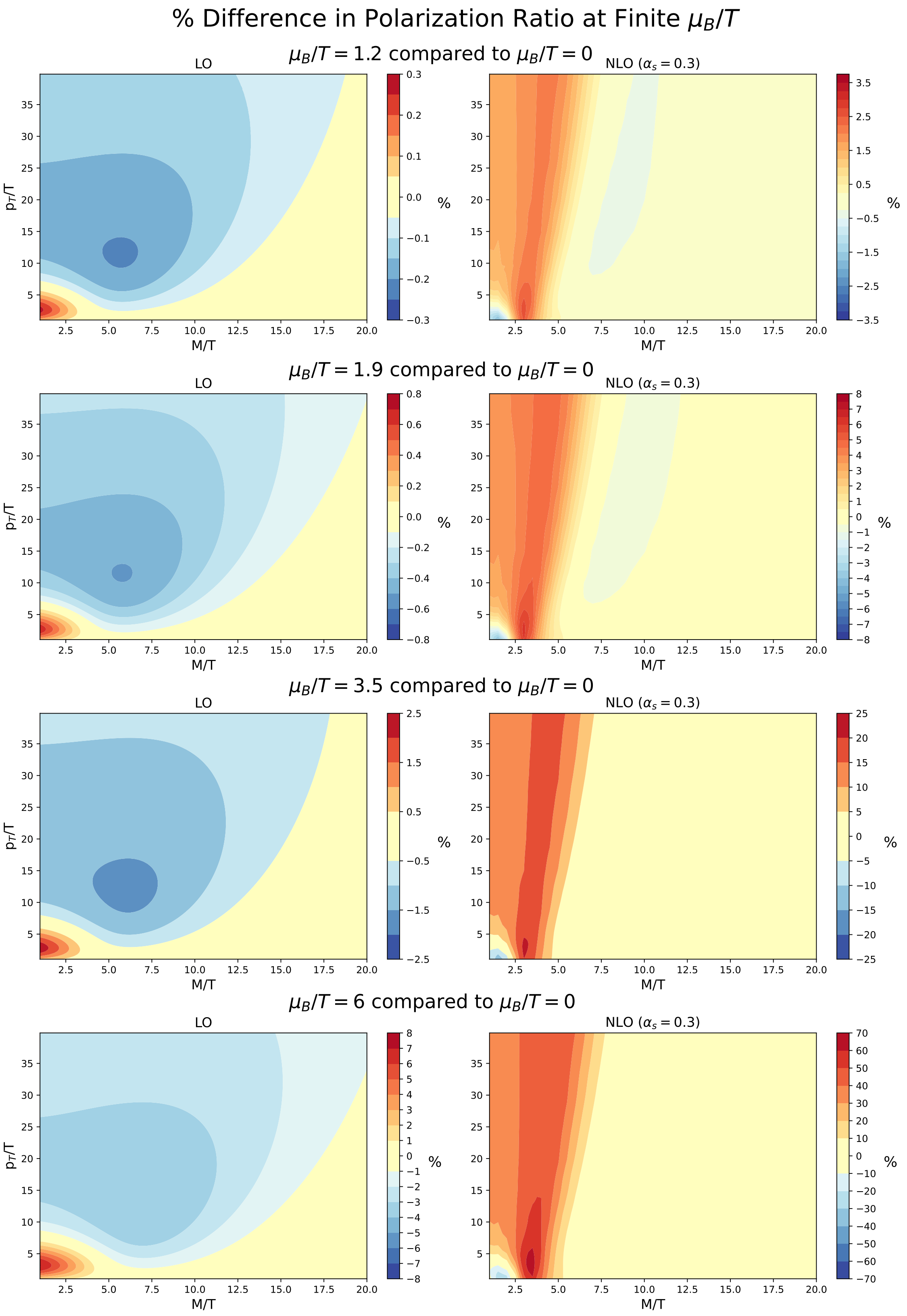

Figure 4.7: 2D contour plots of the percent difference in r_{TL} at finite μ_B relative to $\mu_B = 0$. LO results (left) and NLO results at $\alpha_s = 0.3$ (right) are shown for $\mu_B/T = 1.2$, 1.9, 3.5, and 6.

Chapter 5

Discussion and Conclusions

Dileptons have an important role in probing the early stages of heavy-ion collisions. With future low energy experiments on the horizon [35], accurate predictions of dilepton rates and yields at finite baryon density are needed. Recent progress has been made in NLO pQCD calculations at finite μ_B [1,2,40,41], along with predictions of dilepton yields from integrating the rates over a hydrodynamic model [3,4]. However, the rates themselves had not yet been analyzed in detail. In particular, studies have focused on the invariant mass spectrum, where the rate has been integrated over the momentum space of the dilepton pair. Furthermore, polarized dilepton emission, which can be measured experimentally, had not been thoroughly explored.

This thesis serves as a comprehensive investigation of the structure of 2D differential thermal dilepton rates with respect to invariant mass and transverse momentum. Chapter 2 introduced the kinetic theory formulation of the LO dilepton rate in the thermal QGP stage of HICs. The results of Chapters 3 and 4 were derived from recent pQCD calculations of the finite μ_B dilepton spectral functions at NLO [2]. In Chapter 3, I compared the differential rates at LO and NLO and explored the 2D effect of finite baryon chemical potential for the first time. Finally, in Chapter 4, I performed a similar analysis for the transverse and longitudinally polarized spectral functions. Most importantly, this is the first study of polarized dileptons in the context of finite net baryon density and NLO corrections.

In Chapter 2, I re-derived several expressions for the LO quark-antiquark annihilation contribution to the thermal dilepton rate. Beginning from kinetic theory principles, I first derived the Maxwell-Boltzmann approximation for the fully differential rate with respect to the 4-momentum of the dileptons. I then repeated the derivation with Fermi-Dirac quark distributions in Section 2.3.2 and introduced finite baryon chemical potential in Section 2.3.3. For the Fermi-Dirac rate at finite μ_B, I obtained a more simplified result than previous derivations [45] and showed that these expressions are equivalent. In the Maxwell-Boltzmann case, the contribution of finite μ_B cancels, as shown in Section 2.3.3. These rates were then integrated over the transverse momentum, p_T, to obtain the Lorentz invariant mass spectrum, dR/dM^2, and the results were used to compare the Maxwell-Boltzmann approximation to the Fermi-Dirac results at varying baryon chemical potential. While the p_T integration of the Maxwell-Boltzmann rate could be calculated analytically, the Fermi-Dirac case required numerical methods. Comparison of the invariant mass spectra showed that Maxwell-Boltzmann dilepton distributions are a poor approximation at finite μ_B. Therefore, rates derived from proper Fermi-Dirac statistics are essential for phenomenology of future low energy experiments, which will probe the finite μ_B region.

In Chapter 3, I analyzed the M and p_T structure of the differential rate, dR/d^4P, at LO and NLO. Numerical tables[1] for the longitudinal and transverse spectral functions from [2] were used to calculate the differential rate over a 2D grid of M and p_T values. The results agreed with previous observations, which found that NLO corrections enhance the rate when the invariant mass is small compared to the temperature of the plasma. This is mostly caused by the bremsstrahlung processes that dominate in this limit. Another interesting consequence of bremsstrahlung terms was seen at finite μ_B, where the NLO rate is enhanced rather than suppressed by μ_B in the low M region. Although this enhancement was apparent in the rates, the effect of μ_B was not significant in recent yield calculations [3]. Further study of dilepton yields is needed at lower collision energies, where the effect of μ_B will be stronger.

In Chapter 4, I investigated the 2D effect of μ_B on polarized dilepton emission at LO and NLO. These results demonstrated, for the first time, that NLO corrections radically alter the structure of the polarization compared to the LO case. This is especially interesting in contrast to the total rates in Chapter 3, which were only marginally enhanced by the NLO corrections. The NLO polarizations also show much more dependence on both M and p_T, which can reveal more information about the underlying physics. In light of the large effect of NLO corrections on the dilepton polarization, even higher order pQCD calculations (NNLO) could be considered, together with non-perturbative lattice QCD studies. The results also show that there is much more structural variation in the effect of μ_B on the polarization compared to the rates alone. Furthermore, the transverse and longitudinal components are affected differently by μ_B. For example, one may be enhanced

---

[1] These results were provided by Greg Jackson.

while the other is suppressed. At NLO, there is also cross-over from suppression to enhancement as p_T increases at fixed M. This structural variation with respect to M and p_T is promising for extraction of μ_B from polarized dilepton emission. However, integrating over all p_T, as is typical, will dilute the polarization ratio. An alternate approach could be integrating over smaller p_T bins to isolate regions of enhancement and suppression. One challenge with this approach is that the integrated dilepton rates are already very small. Therefore, without p_T integration, even more collision events will be needed in experiments to measure the differential rates.

In future work, the 2D differential rates studied here can be used in hydrodynamic models to predict the dilepton yield from the thermal QGP stage of low energy HIC experiments. Additionally, the analysis in this work can be extended to dilepton rates from the pre-equilibrium and hadronic stages of HICs. These will be needed to calculate the total dilepton yields and polarizations over the entire evolution of the collision, which can be compared to future dilepton measurements from LHCb [52] and ALICE [53]. This work has also assumed mid-rapidity in the local fluid rest frame and could be generalized further.

Bibliography

[1] G. Jackson. “Shedding light on thermal photon and dilepton production”. *EPJ Web Conf.*, 274, 2022 XVth Quark Confinement and the Hadron Spectrum Conference (ConfXV)(05014), 2022. `doi:10.48550/arXiv.2211.09575`.

[2] Jessica Churchill, Lipei Du, Charles Gale, Greg Jackson, and Sangyong Jeon. “Dilepton production at NLO and intermediate invariant-mass observables”. 11 2023. `arXiv:2311.06675`.

[3] J. Churchill. “Electromagnetic radiation from various stages of heavy-ion collisions”. *Ph.D. thesis, McGill U.*, 2022.

[4] Jessica Churchill, Lipei Du, Bailey Forster, Han Gao, Greg Jackson, Sangyong Jeon, and Charles Gale. “Thermal dilepton production in heavy-ion collisions at beam-energy-scan (BES) energies”. *EPJ Web of Conferences (accepted, in press)*, 12 2023. `arXiv:2312.10166`.

[5] Murray Gell-Mann. “A Schematic Model of Baryons and Mesons”. *Phys. Lett.*, 8:214–215, 1964. `doi:10.1016/S0031-9163(64)92001-3`.

[6] G. Zweig. "An SU(3) model for strong interaction symmetry and its breaking; Version 2". 1964. URL: `http://cds.cern.ch/record/570209`, `doi:10.17181/CERN-TH-412`.

[7] E. M. Riordan. "The Discovery of quarks". *Science*, 256:1287–1293, 1992. `doi:10.1126/science.256.5061.1287`.

[8] Roman Pasechnik and Michal Šumbera. "Phenomenological Review on Quark–Gluon Plasma: Concepts vs. Observations". *Universe*, 3(1):7, 2017. `arXiv:1611.01533`, `doi:10.3390/universe3010007`.

[9] Jana N. Guenther. "Overview of the QCD phase diagram: Recent progress from the lattice". *Eur. Phys. J. A*, 57(4):136, 2021. `arXiv:2010.15503`, `doi:10.1140/epja/s10050-021-00354-6`.

[10] Charles Gale, Sangyong Jeon, and Björn Schenke. "Hydrodynamic modeling of heavy-ion collisions". *International Journal of Modern Physics A*, 28(11):1340011, apr 2013. URL: `https://doi.org/10.1142%2Fs0217751x13400113`, `doi:10.1142/s0217751x13400113`.

[11] Luigi Di Lella and Carlo Rubbia. "The Discovery of the W and Z Particles". *Adv. Ser. Direct. High Energy Phys.*, 23:137–163, 2015. `doi:10.1142/9789814644150_0006`.

[12] H. Fritzsch, Murray Gell-Mann, and H. Leutwyler. "Advantages of the Color Octet Gluon Picture". *Phys. Lett. B*, 47:365–368, 1973. `doi:10.1016/0370-2693(73)90625-4`.

[13] H. Fritzsch. "The History of QCD". *Cern Courier*, 2012.

[14] Michael E. Peskin and Daniel V. Schroeder. *An Introduction to quantum field theory*, pages 78, 490. Addison-Wesley, Reading, USA, 1995.

[15] Matthew D. Schwartz. *Quantum Field Theory and the Standard Model*. Cambridge University Press, 3 2014.

[16] Chen-Ning Yang and Robert L. Mills. "Conservation of Isotopic Spin and Isotopic Gauge Invariance". *Phys. Rev.*, 96:191–195, 1954. `doi:10.1103/PhysRev.96.191`.

[17] Franz Gross et al. "50 Years of Quantum Chromodynamics". *Eur. Phys. J. C*, 83:1125, 2023. `arXiv:2212.11107`, `doi:10.1140/epjc/s10052-023-11949-2`.

[18] Alexandre Deur, Stanley J. Brodsky, and Guy F. de Téramond. "The QCD running coupling". *Progress in Particle and Nuclear Physics*, 90:1–74, sep 2016. URL: `https://doi.org/10.1016%2Fj.ppnp.2016.04.003`, `doi:10.1016/j.ppnp.2016.04.003`.

[19] David J. Gross and Frank Wilczek. "Ultraviolet Behavior of Nonabelian Gauge Theories". *Phys. Rev. Lett.*, 30:1343–1346, 1973. `doi:10.1103/PhysRevLett.30.1343`.

[20] H. David Politzer. "Reliable Perturbative Results for Strong Interactions?". *Phys. Rev. Lett.*, 30:1346–1349, 1973. `doi:10.1103/PhysRevLett.30.1346`.

[21] Vardan Khachatryan et al. "Constraints on parton distribution functions and extraction of the strong coupling constant from the inclusive jet cross section in pp

collisions at $\sqrt{s} = 7$ TeV". *Eur. Phys. J. C*, 75(6):288, 2015. `arXiv:1410.6765`, `doi:10.1140/epjc/s10052-015-3499-1`.

[22] Tapan K. Nayak. "Probing the QCD phase structure using event-by-event fluctuations". *J. Phys.: Conf. Ser.*, 1602:012003, 2020. URL: `http://cds.cern.ch/record/2729160`, `arXiv:2008.04643`, `doi:10.1088/1742-6596/1602/1/012003`.

[23] Patrick Steinbrecher. "The QCD crossover at zero and non-zero baryon densities from Lattice QCD". *Nucl. Phys. A*, 982:847–850, 2019. `arXiv:1807.05607`, `doi:10.1016/j.nuclphysa.2018.08.025`.

[24] Claudia Ratti. "Lattice QCD and heavy ion collisions: a review of recent progress". *Rept. Prog. Phys.*, 81(8):084301, 2018. `arXiv:1804.07810`, `doi:10.1088/1361-6633/aabb97`.

[25] Michael Strickland. "Small system studies: A theory overview". *Nuclear Physics A*, 982:92–98, 2019. `doi:10.10/j.nuclphysa.2018.09.071`.

[26] Rajeev S. Bhalerao. "Relativistic heavy-ion collisions". In *1st Asia-Europe-Pacific School of High-Energy Physics*, pages 219–239, 2014. `arXiv:1404.3294`, `doi:10.5170/CERN-2014-001.219`.

[27] Chun Shen, Zhi Qiu, Huichao Song, Jonah Bernhard, Steffen Bass, and Ulrich Heinz. "The iEBE-VISHNU code package for relativistic heavy-ion collisions". 2015. `arXiv:1409.8164`.

[28] F. D. Aaron et al. "Combined Measurement and QCD Analysis of the Inclusive e+- p Scattering Cross Sections at HERA". *JHEP*, 01:109, 2010. `arXiv:0911.0884`, `doi:10.1007/JHEP01(2010)109`.

[29] François Gelis. "Color Glass Condensate and Glasma". *International Journal of Modern Physics A*, 28:1330001, 2013. URL: `https://doi.org/10.1142%2Fs0217751x13300019`, `doi:10.1142/s0217751x13300019`.

[30] Bjoern Schenke, Prithwish Tribedy, and Raju Venugopalan. "Fluctuating Glasma initial conditions and flow in heavy ion collisions". *Phys. Rev. Lett.*, 108:252301, 2012. `arXiv:1202.6646`, `doi:10.1103/PhysRevLett.108.252301`.

[31] Björn Schenke, Sangyong Jeon, and Charles Gale. "$(3+1)$D hydrodynamic simulation of relativistic heavy-ion collisions". *Physical Review C*, 82(1), jul 2010. URL: `https://doi.org/10.1103%2Fphysrevc.82.014903`, `doi:10.1103/physrevc.82.014903`.

[32] Fred Cooper and Graham Frye. "Comment on the Single Particle Distribution in the Hydrodynamic and Statistical Thermodynamic Models of Multiparticle Production". *Phys. Rev. D*, 10:186, 1974. `doi:10.1103/PhysRevD.10.186`.

[33] S. Ryu, J. F. Paquet, C. Shen, G. S. Denicol, B. Schenke, S. Jeon, and C. Gale. "Importance of the Bulk Viscosity of QCD in Ultrarelativistic Heavy-Ion Collisions". *Phys. Rev. Lett.*, 115(13):132301, 2015. `arXiv:1502.01675`, `doi:10.1103/PhysRevLett.115.132301`.

[34] Sangwook Ryu, Jean-François Paquet, Chun Shen, Gabriel Denicol, Björn Schenke, Sangyong Jeon, and Charles Gale. "Effects of bulk viscosity and hadronic rescattering in heavy ion collisions at energies available at the BNL Relativistic Heavy Ion Collider and at the CERN Large Hadron Collider". *Phys. Rev. C*, 97(3):034910, 2018. `arXiv:1704.04216`, `doi:10.1103/PhysRevC.97.034910`.

[35] C. Ahdida et al. "Letter of Intent: the NA60+ experiment". 12 2022. `arXiv:2212.14452`.

[36] Frank Geurts and Ralf-Arno Tripolt. "Electromagnetic probes: Theory and experiment". *Prog. Part. Nucl. Phys.*, 128:104004, 2023. `arXiv:2210.01622`, `doi:10.1016/j.ppnp.2022.104004`.

[37] Ulrich W. Heinz and Kang Seog Lee. "The rho peak in the dimuon spectrum as a clock for fireball lifetimes in relativistic nuclear collisions". *Phys. Lett. B*, 259:162–168, 1991. `doi:10.1016/0370-2693(91)90152-G`.

[38] Ralf Rapp and Hendrik van Hees. "Thermal Dileptons as Fireball Thermometer and Chronometer". *Phys. Lett. B*, 753:586–590, 2016. `arXiv:1411.4612`, `doi:10.1016/j.physletb.2015.12.065`.

[39] Charles Gale, Jean-François Paquet, Björn Schenke, and Chun Shen. "Multimessenger heavy-ion collision physics". *Phys. Rev. C*, 105(1):014909, 2022. `arXiv:2106.11216`, `doi:10.1103/PhysRevC.105.014909`.

[40] G. Jackson. "Two-loop thermal spectral functions with general kinematics". *Phys. Rev. D*, 100(116019), 2019. `doi:10.1103/PhysRevD.100.116019`.

[41] G. Jackson, M. Laine. "Testing thermal photon and dilepton rates". *JHEP*, 1911(144), 2019.

[42] K. Kajantie, Joseph I. Kapusta, Larry D. McLerran, and A. Mekjian. "Dilepton Emission and the QCD Phase Transition in Ultrarelativistic Nuclear Collisions". *Phys. Rev. D*, 34:2746, 1986. `doi:10.1103/PhysRevD.34.2746`.

[43] J. I. Kapusta and Charles Gale. *Finite-temperature field theory: Principles and applications*. Cambridge Monographs on Mathematical Physics. Cambridge University Press, 2011. `doi:10.1017/CBO9780511535130`.

[44] David Griffiths. *Introduction to elementary particles*. Wiley-VCH, Weinheim, 2nd, revised edition, 2008.

[45] A. Dumitru, D. H. Rischke, Th. Schönfeld, L. Winckelmann, H. Stöcker, and W. Greiner. "Suppression of Dilepton Production at Finite Baryon Density". *Phys. Rev. Lett.*, 70:2860, 1993.

[46] C. Gale and J. I. Kapusta. "Vector dominance model at finite temperature". *Nucl. Phys. B*, 357(10):65—-89, 1991.

[47] H. A. Weldon. "Simple rules for discontinuities in finite temperature field theory". *Phys. Rev. D 42*, 42(10):2384–2387, 1990.

[48] P. Aurenche, F. Gelis, G. D. Moore, and H. Zaraket. "Landau-Pomeranchuk-Migdal resummation for dilepton production". *JHEP*, 12:006, 2002. `arXiv:hep-ph/0211036`,`doi:10.1088/1126-6708/2002/12/006`.

[49] M. Arslandok et al. “Hot QCD White Paper”. 3 2023. `arXiv:2303.17254`.

[50] L. Du. “Hydrodynamic description of the baryon-charged quark-gluon plasma”. *Ph.D. thesis, Ohio State U.*, 2021.

[51] Hualong Gervais and Sangyong Jeon. “Photon Production from a Quark-Gluon-Plasma at Finite Baryon Chemical Potential”. *Phys. Rev. C*, 86:034904, 2012. `arXiv:1206.6086`, `doi:10.1103/PhysRevC.86.034904`.

[52] I. Bediaga et al. “Physics case for an LHCb Upgrade II - Opportunities in flavour physics, and beyond, in the HL-LHC era”. 2019. `arXiv:1808.08865`.

[53] D. Adamová et al. “A next-generation LHC heavy-ion experiment”. 2019. `arXiv:1902.01211`.